University of Alberta

SYNTHESIS, CHARACTERIZATION, AND DIELECTROPHORETIC ASSEMBLY OF METAL-OXIDE NANOWIRES

by

Michael Lau

A thesis submitted to the Faculty of Graduate Studies and Research in partial fulfillment of the requirements for the degree of **Master of Science**

in

Micro-Electrical-Mechanical Systems (MEMS) and Nanosystems

Department of Electrical and Computer Engineering

Edmonton, Alberta

Fall 2008

Library and Archives Canada

Published Heritage Branch

395 Wellington Street
Ottawa ON K1A 0N4
Canada

Bibliothèque et Archives Canada

Direction du Patrimoine de l'édition

395, rue Wellington
Ottawa ON K1A 0N4
Canada

Your file Votre référence
ISBN: 978-0-494-47290-3
Our file Notre référence
ISBN: 978-0-494-47290-3

NOTICE:
The author has granted a non-exclusive license allowing Library and Archives Canada to reproduce, publish, archive, preserve, conserve, communicate to the public by telecommunication or on the Internet, loan, distribute and sell theses worldwide, for commercial or non-commercial purposes, in microform, paper, electronic and/or any other formats.

The author retains copyright ownership and moral rights in this thesis. Neither the thesis nor substantial extracts from it may be printed or otherwise reproduced without the author's permission.

AVIS:
L'auteur a accordé une licence non exclusive permettant à la Bibliothèque et Archives Canada de reproduire, publier, archiver, sauvegarder, conserver, transmettre au public par télécommunication ou par l'Internet, prêter, distribuer et vendre des thèses partout dans le monde, à des fins commerciales ou autres, sur support microforme, papier, électronique et/ou autres formats.

L'auteur conserve la propriété du droit d'auteur et des droits moraux qui protège cette thèse. Ni la thèse ni des extraits substantiels de celle-ci ne doivent être imprimés ou autrement reproduits sans son autorisation.

In compliance with the Canadian Privacy Act some supporting forms may have been removed from this thesis.

While these forms may be included in the document page count, their removal does not represent any loss of content from the thesis.

Conformément à la loi canadienne sur la protection de la vie privée, quelques formulaires secondaires ont été enlevés de cette thèse.

Bien que ces formulaires aient inclus dans la pagination, il n'y aura aucun contenu manquant.

Canada

Abstract

Modern gas detection in commercial, industrial, and medical applications all necessitate the use of precise and accurate sensors. Nanowire gas sensor arrays engineered by dielectrophoresis potentially offer highly sensitive gas detection with massively parallel fabrication. TiO_2/TiO_x nanowires were synthesized by the Vapor-Liquid-Solid (VLS) growth mechanism. SEM images revealed nanowire dimensions of 80-100 nm in diameter and several microns in length. Elemental composition and crystal lattice structure were confirmed by XPS and AES, and XRD and TEM, respectively. Dielectrophoresis was performed on gold and zinc oxide (ZnO) nanowires. Both materials were successfully assembled onto electrode arrays, with the single nanowire assembly of gold nanowires and multiple nanowire assembly of zinc oxide.

Acknowledgements

Firstly, I would like to Dr. Stephane Evoy for providing me with the opportunity to perform this M.Sc. project under his guidance. The gift of a higher education cannot be understated. I would also like to thank the other members of my defense committee, Dr. Mark McDermott and Dr. Vien Van, for giving me a chance to present my work.

Secondly, further acknowledgements go out to the University of Alberta, the Department of Electrical and Computer Engineering, and the National Institute of Nanotechnology for their institutional presence. Added thanks must be given to NINT, as they have provided a desk, lab space, and -- most importantly – funding for this project.

Facilities acknowledgements go out to the University of Alberta Nanofabrication Facility, as 90% of this project would not be possible without their equipment and training. Countless thanks go toward Dr. Mark McDermott lending me the use of his lab and 3-Zone RF furnace. The NINT Electron Microscopy lab and the X-Ray characterization lab are also acknowledged for their invaluable use in characterizing my results. The Alberta Center for Surface Engineering and Sciences must also be thanked for providing XPS and AES scans.

The support from family and friends cannot be acknowledged enough, and are too numerous to count. In particular, my twin brother Billy by inspiring me with his unlimited genius and ambition that I can never hope to match.

Lastly, I would like to thank the one thing that has kept me going through the past seven years of school: coffee. Infinitely dependable and tastes great! ☺ Well, not really, but at least my sense of humor is still intact!

Table of Contents

1 Introduction 1

2 Literature Review 5

2.1. Volatile Gas Sensing 5

2.2. VLS Nanowire Synthesis 9

2.2. Properties of TiO_2/TiO_x 11

2.3. TiO_2 VLS Nanowire Synthesis 12

2.4. Dielectrophoresis 14

2.4.1. Dielectrophoretic Manipulation of a Nanowire 17

3 Synthesis and Characterization of TiO_2/TiO_x Nanowires 20

3.1. Experimental Goals 20

3.2. Experimental Design 21

3.2. Experimental Results 23

3.2.1. Initial Optimization of Nanowire Growth Parameters 23

3.2.2. Refinement Towards Rutile and Further Characterization 26

3.2.3. Improvement of Yield 29

3.3. Discussion of Results 34

3.4. Summary 37

4 Dielectrophoretic Assembly of Nanowires 38

4.1. Experimental Goals 38

4.2. Types of Nanowires 39

4.3. Experimental Design 40

4.4.1. Iteration 1: Nanowire Assembly Under Vibrational Environments 42

4.4.2. Iteration 2: Nanowire Assembly Under Quiet Environments 46

4.4.3. Iteration 3: Assembly of ZnO Nanowires 48

4.5. Discussion of Results 51

4.5.1. Dielectrophoresis and Electrorotation 52

4.5.2. Other Frequency Response Issues 54

4.5. Summary 55

5 Conclusion 56

References 60

List of Figures

Figure 1 Grain size dependence of conductivity 7

Figure 2: Illustration of the Vapor-Liquid-Solid nanowire growth mechanism. 10

Figure 3: A general diagram of the experimental setup 21

Figure 4: Successful nanowire growth using a mechanical grade wafer 24

Figure 5: XRD Scan of mechanical grade wafer experiment 25

Figure 6: Successful nanowire growth using prime grade wafer. 26

Figure 7: XRD scan of prime grade wafer experiment 27

Figure 8: Surface characterization of prime grade wafer experiment 28

Figure 9: Effect of oxide thickness 30

Figure 10: Effect of surface roughness with a 65 nm oxide layer 30

Figure 11: Effect of influx pressure 32

Figure 12: XRD scan of 65nm oxide sample 33

Figure 13: TEM image and electron diffraction analysis 33

Figure 14: STEM images of nanowire and nucleus 34

Figure 15: Decomposition of thin oxides 35

Figure 16: Illustration of the proposed growth process. 36

Figure 17: Decomposition of thick oxides 36

Figure 18: Gold nanowires synthesized through template electroplating 39

Figure 19: ZnO oxide nanowires synthesized by PVD methods 40

Figure 20: Dielectrophoretic assembly process 41

Figure 21: Process flow for the creation of dielectrophoretic assembly finger electrodes with capacitve coupling (Mask design 1) 43

Figure 22: Single electrode pads with finger electrodes (Mask design 2) 44

Figure 23: Single layer assembly electrodes (Mask design 3) 45

Figure 24: Nanowire assembly with third mask 46

Figure 25: Vibrational effects on a gold nanowire solution 46

Figure 26: Assembly of nanowires at 35 V_{pp} and 1 MHz 47

Figure 27: Single nanowire assembly of gold nanowires 48

Figure 28: Overview of second-generation single layer assembly electrodes (Mask Design 4) 49

Figure 29: Dielectrophoretic assembly of ZnO nanowires 50

Figure 30: Dielectrophoretic assembly of a segmented nanowire 58

List of Abbreviations and Elemental Names

AES	Auger Electron Spectroscopy
Au	Gold
BOE	Buffered Oxide Etch
CMOS	Complementary Metal-Oxide Semiconductor
DI	De-Ionized
FIB	Focused Ion Beam
KI	Potassium-Iodine
I	Iodine
PEDOT/PSS	poly(3,4-ethylenedioxythiophene)/poly(styrenesulfonate)
ppm	parts per million
SEM	Scanning Electron Microscopy
SiC	Silicon Carbide
SLS	Solid-Liquid-Solid
TEM	Transmission Electron Microscopy
Ti	Titanium
TiN	Titanium Nitride
TiO	Titanium Oxide
TiO_2	Titanium Dioxide
TiO_x	Titanium Oxide of different oxygen content
UV	Ultraviolet
VLS	Vapor-Liquid-Solid

VS	Vapor-Solid
XPS	X-Ray Photoelectron Spectroscopy
XRD	X-Ray Diffraction
ZnO	Zinc Oxide

1 Introduction

Modern instrumentation necessitates the use of precise sensors in order to retrieve information from the surrounding environment. The usage of gas sensors in industrial, commercial, and medical industries all require the specific detection of certain molecules in order to maintain efficient device operation or to provide accurate diagnoses. For instance, gaseous hydrocarbons and hydrogen sulfide are compounds whose presence and absence are critical to throughput and safety in the oil industry. Gas sensors are also important for detecting carbon monoxide in households and monitoring oxygen concentrations in an automobile engine. Medical applications suffer from balancing expensive and cumbersome devices with accurate detection of disease markers. For example, patients with diabetic ketoacidosis exhale acetone in parts-per-million

concentrations [1], of which current detection methods involve the utilization of cumbersome gas chromatographers.

Engineering gas sensors often involves a set of trade-offs including cost, size, sensitivity, and specificity. For instance, acetone shares a conduction response with ethanol and thus raises the need for specificity. The problem of false positives can be addressed by using multiple sensors that are 'tuned' to particular analytes for the purpose of generating a fingerprint. However, the cost of this approach quickly becomes prohibitive with additional sensors and electronics. Non-obvious supporting technologies such as heating elements and power sources now become significant factors, adding both cost and complexity to the system. These drawbacks therefore necessitate the development of integrated and inexpensive gas detection technologies.

Nanoscale gas sensors, and in particular nanowire gas sensor arrays, have become a potential platform that can provide sensitive and accurate detection while simultaneously providing cost and size advantages in the form of massively parallel fabrication. Nanoscale control of grain sizes and doping levels offer significantly higher levels of sensitivity unavailable to conventional technologies. Nanowire gas sensors offer additional surface area to volume ratio advantages as compared to competing nanoscale technologies, allowing even highly dilute analytes to produce large changes within the nanowire's structure. However, the assembly of nanowires often requires direct physical manipulation at nanometer scales, of which the technology is as of yet relatively undeveloped. Bottom-up fabrication techniques are time consuming and require the precise orientation of a nanowire beforehand. Non-mechanical techniques such as functionalization and DNA scaffolding can assemble nanostructures at the cost of

complex surface chemistries and interactions [2]. Magnetophoresis offers macroscale manipulation of nanowires through magnetic fields, though limited to a specific range of materials [3-5]. Dielectrophoresis is the favored option as it can manipulate neutral particles by using electric field gradients [6]. Top-down parallel assembly of nanowires on top of several pre-fabricated electrodes can be generated by the application of an electric potential. Highly dense nanoscale sensor arrays can thus be potentially made quickly and efficiently.

A suitable material for this sensor platform is titanium oxide (TiO_2), since it is sensitive to both acetone and ethanol, as well as a wide variety of other commercially applicable gases such as H_2, O_2, NO_2, and CO [7]. As a nanowire, TiO_2 is a relatively uninvestigated material when synthesized through physical vapor deposition (PVD) vapor-liquid-phase (VLS) methods, with only a small number of groups actively pursuing this avenue of research. Previous work in this field done by other groups involved the pre-deposition of a critical titanium-based layer [8-13] of which the specific growth mechanism is unclear. Therefore, the major contribution of the work presented in this thesis is to establish a method whereby such a titanium-based layer is rendered unnecessary and to clarify the specific growth mechanism in this process. Various synthesis parameters will also be investigated to determine the critical factors affecting the yield of nanowire growth.

Finally, in order to move towards a nanowire gas-sensing platform, this thesis will also investigate the use of dielectrophoresis in an effort to assemble single nanowires across two electrodes. Assembly of gold and zinc oxide nanowires are investigated concurrently with TiO_2 nanowire synthesis to provide an experimental basis for the future

assembly of TiO2/TiOx nanowires. Different electrode designs are utilized, as well as an optimization of voltage and frequency parameters, to obtain a suitable process flow for nanowire assembly.

2 Literature Review

2.1. Volatile Gas Sensing

Gas sensor operation relies on a specific material property change due to a change in the ambient environment. For example, a change in resistance within a thin film can be directly correlated with the amount of gas analyte within the entire system. The sensing mechanism usually involves the donation of an electron by an adsorbed reducing gas species and results in an increase in the gas sensor's conductivity. Similarly, an oxidizing gas species would remove an electron from the sensor and result in a decrease in conductivity. The addition of vacancy sites plays an important role as any newly occupying species would greatly change the overall conductivity [7].

The majority of gas sensors in the academic and commercial environment are based on thin-film technologies. The reasons range from cost-effectiveness to ease of

production as thin films can be sputtered or sintered onto a sensing platform [7]. Properties such as response time and sensitivity can be altered with thin film technologies as compared to their respective bulk counterparts. Metal oxides are the most popular class of materials because of their ease of processing, overall stability, and wide range of sensitivities. In particular, tin oxide has been widely investigated to detect a variety of gases, such as carbon monoxide (CO) and hydrogen (H_2) [7]. Other metal oxide materials include zinc oxide for the detection of oxygen and volatile organic vapors [7].

Thin film technologies, typically on the order of hundreds of nanometers to micrometers in thickness, enable critical parameters to be easily manipulated in order to alter sensor performance. For instance, the response of a metal-oxide gas sensor is dependent on the material's grain size D and the Debye length L (Fig. 1) [14-16]. An increase in sensor response and sensitivity can be created by elevated temperatures, which increases the characteristic Debye length. Sensor activity can be further enhanced by the addition of dopants to further reduce the Debye length [7,15]. A similar response can instead be generated by grain size control. Large grain sizes result in the main conduction mode being along the grain boundaries, overcoming surface potentials to travel from one grain to the next (Fig. 1a). Reducing D to the same order as 2L results in a high resistance channel-based conduction mode between grains, which is constricted by the same surface potential as before (Fig. 1b). Further reduction in D results to below 2L leads to surface conduction over the grain, leading to fast electron conduction and increased sensitivity (Fig. 1c).

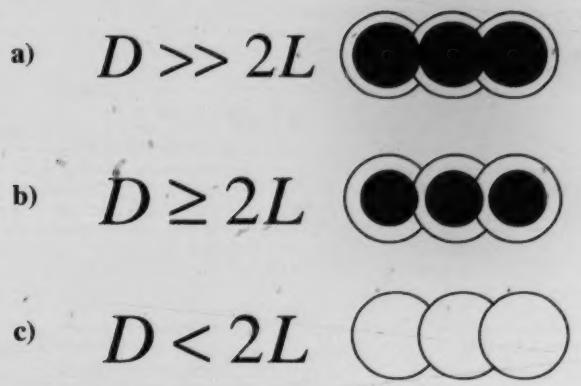

Figure 1 Grain size dependence of conductivity

a) When the grain size diameter is much greater than twice the Debye length, electrons from donated gas species mainly conduct through the grain boundary defects. b) As the grain boundary decreases to the same order as the Debye length, conduction becomes neck controlled as it is dominated by individual molecules. c) Once the grain size is below twice the Debye length, the entire grain becomes depleted and any donated electrons will experience fast conduction and will create a surface conduction effect [14,15].

Integrated gas sensors are advantageous as supporting technologies can be supported or enhanced on a single platform. Onboard CMOS circuitry can process and condition the obtained sensor information. Heating elements can be directly incorporated within the sensor array. Supporting power electronics are minimized due to lower power consumption. One such implementation of integrated sensor technology has been pioneered by the Semancik group with thin film technologies [17-21]. Microheaters and CMOS circuitry were successfully implemented with tin oxide thin films to create a completely integrated sensing platform.

However, there are many drawbacks with metal oxide thin film gas sensors. Sensitivity is the most critical issue as current achievable limits are at the parts-per-million range [7] while researchers would like to move into the parts-per-billion range. This level of detection is difficult to achieve with thin-film technologies, due to its bulk

size and low surface area-to-volume ratio [22]. Integrating multiple sensors onto a single platform becomes problematic as the overall complexity increases with multiple masking, alignment, and removal steps. Scaling up microheater technologies becomes difficult as the process adds even more steps to an already complicated process [17-23,24].

These limitations have pushed researchers towards nanowire gas sensors as they potentially offer increased sensitivity to gas detection due to their surface-area-to-volume ratio. Similar to thin film technologies, control over nanowire diameters enable them to be smaller than the Debye length and thus increasing their response and sensitivity [14-15]. Both tin oxide [22,25] and zinc oxide [26-27] nanowire gas sensors can detect H_2, CO, and volatile organics at tens of ppm ranges.

The scale of the nanowires also enables them to be incorporated within novel sensor platforms. Highly-dense nanowire sensor arrays of different material compositions can be assembled to allow room for additional integrated circuitry [28]. Other possibilities include operating a nanowire similar to a transistor as demonstrated by Li *et al* with ZnO [29] by monitoring any changes in current caused by the presence of oxygen affecting the depletion region.

A variety of growth methods ranging from templated electroplating to vapor-liquid-solid (VLS) catalytic synthesis are available for nanowire synthesis [30]. Zinc oxide nanowires and other nanostructures have been synthesized through the VLS growth mechanism several times and their responses to oxygen and hydrogen have been measured [26-27,29,31]. Tin oxide nanowire sensors have also been synthesized by electroplating and their responses to H_2 and CO have been reported [22-25]. More

recently, Dan *et al* have used templated electroplating to produce segmented nanowires of gold and PEDOT/PSS [32].

2.2. VLS Nanowire Synthesis

The science behind the vapor-liquid-solid (VLS) growth of nanowires owes itself to Wagner and Ellis' landmark publication in 1964 on the synthesis of silicon whiskers [33]. Research has since progressed into various other material compositions and nanostructures as reviewed by Law *et al* [30]. The mechanism involves the use of a catalyst particle serving as a growth seed and chosen for properties such as solubility and eutectic points. Temperatures are elevated to bring the catalyst into a liquid phase while source vapors flow diffuse into the particle and saturate it with the source material. The catalyst quickly becomes supersaturated and starts to crystallize the excess material outside of the particle. Further precipitation occurs to form a 1-D nanowire, of which the diameter is dependent on the nanoparticle's size (Fig. 2).

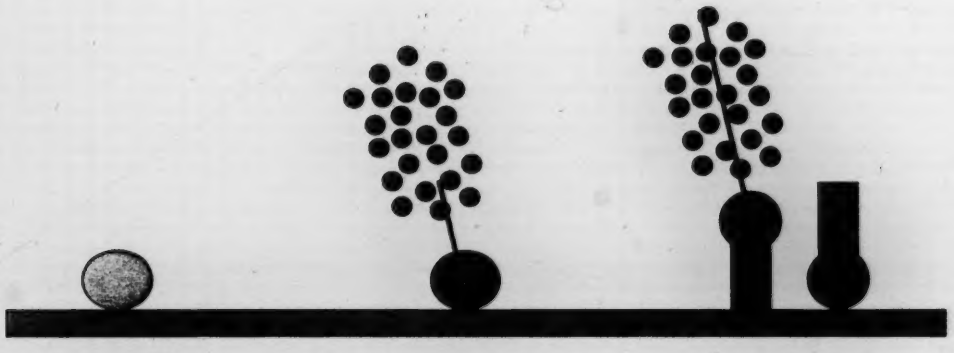

Figure 2: Illustration of the Vapor-Liquid-Solid nanowire growth mechanism.

Source vapors flow towards the liquid catalyst droplet. The particle quickly saturates and precipitates the excess material as a 1-D structure. The nanowire structure can push the catalyst away from the substrate depending on the existence of any expitaxial growth mechanisms in the system.

A eutectic point between the source material and catalyst renders high temperatures unnecessary and makes the process solely dependent on the availability of source vapors. Alternative catalytic pathways are possible through a Solid-Liquid-Solid (SLS) growth mechanism whereby the primary source for material is diffusion from a supporting layer. Vapor-Solid mechanisms are another possibility, whereby nanowires and similar structures form from spontaneous nucleation and hence do not a need catalyst particle [8-11,30].

Many indirect factors can influence nanowire synthesis. Surface roughness is one such example, as hillocking and defects on the growth surface may serve as local nucleation sites. The growth of zinc oxide (ZnO) nanowires has been shown to grow on such sites [34-35]. Melting point depression is another factor since all materials exhibit a lower melting point as the diameter of the particle decreases [36]. Lowering the reaction temperature may help to avoid unwanted high temperature reactions but also alters

critical properties such as diffusion and reactivity. Catalyst poisoning may occur or even the formation of amorphous SiO_2 nanowires [37-38].

2.2. Properties of TiO_2/TiO_x

Titanium Dioxide (TiO_2) is a common material with many applications, from commercial usage as a white pigment to industrial applications as a photocatalyst [39]. Modern solar research incorporates organic dyes into TiO_2 solar cell technologies to boost their efficiency [39-40]. Additionally, its photocatalytic properties create a super-oxidative effect when exposed to UV light. This property has allowed for the design of passive water treatment plants in third-world countries. However, this design has proven to be ineffective since natural UV content in sunlight is only around 3% [39].

Ethanol and acetone are both detectable by TiO_2 gas sensors, as well as oxygen, hydrogen, carbon monoxide [7]. Similar to other metal oxide sensors, altering the grain size greatly reduces its operating temperature. Out of the three possible phases for TiO_2, the rutile phase is favored for gas sensing applications over anatase and brookite due to its overall stability [7]. However, the main drawback is the high synthesis temperature and can lead to unwanted high temperature reactions.

One uncommon form of titanium oxide is TiO/TiO_x. Unlike rutile or anatase, TiO/TiO_x exhibits a rock salt or monoclinic FCC-like structure instead of a tetrahedral one [41-43]. This crystal structure also has regular oxygen vacancies occuring uncommon to TiO_2 [41]. Additionally, TiO/TiO_x is a purely synthetic material and is often made by sintering rutile TiO_2 and titanium together [42]. Rutile phases can also be produced by

heat treatments under the presence of oxygen [43]. Lastly, unlike TiO_2, TiO/TiO_x is conductive and puts it in a unique class of metal oxides [42].

2.3. TiO_2 VLS Nanowire Synthesis

The existing base of literature for TiO_2 nanowire synthesis using VLS growth mechanisms is sparse at best. Wu *et al* reported on the growth of TiO_2 nanowires by several different methods [8-11]. Metallic vapors were produced from titanium powders inside a two-zone furnace with 1050 °C at the high temperature zone and were carried to the low temperature substrate zone at 850 °C. Their initial experiments focused on a two step process where titanium powders were pre-oxidized on top of a silicon substrate before re-exposing the sample to titanium vapors [8]. Subsequent experiments employed a sputtered titanium layer with and without gold, both of which resulted in successful growth of near-identical nanostructures [9-11]. The resulting nanowires for all experiments were identified as single crystal rutile structures.

However, the growth processes described seemed closer to a VS rather than a VLS mechanism. Titanium vapors are unlikely to enter a gold catalyst particle at a temperature lower than its melting point and thus the gold-titanium binary formation point [44]. Condensation effects are more likely due to the low temperature zone and would result in spontaneous nucleation onto the polycrystalline TiO_2 layer. Indeed, all of Wu *et al*'s work taken together does not produce a clear correlation between gold and nanowire formation since no clear difference can be made to their non-catalytic experiments.

Concurrent attempts at single crystal rutile nanowires were made by Xiang *et al* and Zhang *et al* (same group) by using bare wafers and Ti vapors evaporated in one zone at 850 °C [45-46]. Their growth mechanism is described to be the formation of $TiSi_x$ islands which served as a catalyst for the nanowire growth process. The growth mechanism is similar to Wu *et al* in that it is most likely a vapor-solid mechanism of some sort. However, their process raises many questions such as the lack of titanium vapors at low temperatures. Additionally, their own analyses do not agree with their hypothesis since their EDS line scans do not match the suggested $TiSi_x$ stoichiometry. Furthermore, they do they have any diffractive analyses with either XRD or TEM that points toward the formation of $TiSi_x$ crystallites.

Further work was done by Lee *et al* on the growth of TiO_2 nanowires at high temperatures [12]. Similar to Wu *et al* [10-11], a titanium buffer layer with gold on top was used in a single zone RF furnace at 1050 °C. In contrast, the VLS mechanism is likely here since the reaction temperature is comparable to the melting point of gold. The possibility of VS growth is also reduced because of the lack of low temperature condensation effects. Interestingly, the substrate may play an indirect role as TiO_2 nanowires grown on quartz exhibited higher orders of crystallinity than ones grown on sapphire.

In 2006, Dupuis *et al* successfully synthesized rutile TiO_2 nanowires by using a $Ni/TiN/SiO_2$ system at 900 °C [13]. The experiments were novel since they used the *decomposition* of the TiN layer as the titanium source rather than the influx of metallic vapors. Their growth mechanism was facilitated by the existence of trace oxygen occurring within the system and by the reduction effects of hydrogen. Extensive controls

and analyses were made to confirm the unique mechanism, complete with HRTEM images of the catalyst nickel catalyst particle. However, the nanowires were extremely short compared to other groups because of the limited amount of titanium available through the TiN layer.

Additional work was performed using the evaporation of metal-organic titanium powders. Wu and Yu successfully created TiO_2 nanorod and nanowall structures by evaporating titanium acetylacetonate onto non-catalyzed silicon and silica [47]. The experiments were performed in a two-zone furnace by evaporating the metal-organic powder at 200 °C and carrying the vapors to a high temperature zone at 500-700 °C. The resulting nanorod structures lacked a favorable aspect ratio and oddly resembled the columnar structure of a sputtered film. Other groups, such as Pradhan *et al* [48] and Plugaru *et al* [49], had also demonstrated TiO_2 nanorod growth by using metal-oxide sources, but of lower quality compared to all work presented so far.

2.4. Dielectrophoresis

Due to their nanoscale dimensions, nanowires are more efficiently assembled using a macroscale technique rather than through their individual manipulation. As reviewed by Pohl [6], dielectrophoresis is the manipulation of neutral particles using electric field gradients, as opposed to electrophoresis and the manipulation of charged particles by any electric field. Applying an electric potential between two co-planar electrodes induces attractive forces that can be used to assemble a bridging nanowire. Single nanowire assembly is advantageous since it would offer increased sensitivity

through one nanowire that would otherwise be decreased with additional assembled nanowires.

Dielectrophoresis is derived from the fundamental dipole force equation by expressing the force in terms of an effective dipole moment and a gradient in electric field [50]:

$$F_{DEP} = p_{eff} \cdot \nabla \vec{E} \qquad \ldots(1)$$

The effective dipole moment p_{eff} can be expressed in different ways depending on the geometry of the manipulated object. For example, the classic equation for the dielectrophoretic force on a spherical particle is [50]:

$$F_{DEP} = 2\pi\varepsilon_1 r^3 \frac{\varepsilon_2 - \varepsilon_1}{\varepsilon_2 + 2\varepsilon_1} \nabla E^2 \qquad \ldots(2)$$

where the factor $\frac{\varepsilon_2 - \varepsilon_1}{\varepsilon_2 + 2\varepsilon_1}$ is known as the Clausius-Mossotti factor K [6,50], r is the radius of the sphere, and ε_1 and ε_2 are the permittivity of the medium and particle, respectively. The equation can be further expanded for greater accuracy at the expense of greater computational complexity. For instance, higher-order terms can be included to account for highly non-uniform fields due to multipoles and complex geometries [50]. Additionally, the effective dipole moment for certain structures differs depending on the geometrical approximation used. For example, Boote and Evans used an exact cylindrical factor of $\pi r^2 l$ for the effective dipole of a gold nanowire [51]. On the other hand, Jones reported on the use of prolate ellipsoids for approximating needle-like structures,

resulting in higher degrees of accuracy for both higher order differentiation terms and alignment towards the field [50].

Dielectrophoretic force can be attractive or repulsive depending on whether the permittivity of the object or medium is greater or smaller. Conductivity, along with frequency, can be considered by absorbing it into a complex term $\varepsilon + j\sigma/\omega$ where σ is the conductivity of the material and ω is the radial frequency. Since the dielectrophoretic force would only be dependent on the real part of the equation, the Clausius-Mossotti factor K can then be expanded into [50]:

$$\mathrm{Re}[K] = \frac{\varepsilon_2 - \varepsilon_1}{\varepsilon_2 + 2\varepsilon_1} + \frac{3(\varepsilon_1\sigma_2 - \varepsilon_2\sigma_1)}{\tau_{MW}(\sigma_2 + 2\sigma_1)^2(1 + \omega^2\tau_{MW}^2)} \qquad \ldots(3)$$

where τ_{MW} is the Maxwell-Wagner charge relaxation time constant:

$$\tau_{MW} = \frac{\varepsilon_2 + \varepsilon_1}{\sigma_2 + 2\sigma_1} \qquad \ldots(4)$$

Similarly, attractive or repulsive forces are generated depending on whether the conductivity of the object or medium is greater or smaller. The Maxwell-Wagner time constant defines the regions at which either conduction or permittivity dominates Re[K]. Conduction dominates at frequencies where $\omega\tau_{MW} << 1$, whereas permittivity dominates at $\omega\tau_{MW} >> 1$. [50].

A common misconception is that these properties are linear with applied frequency for any material. This assumed linearity is often *not* the case, as biological materials is one such example of a non-linear material [6,50]. Furthermore, many inorganic materials are anisotrophic and have properties dependent on the axis of alignment [50]. Another misconception is that dielectrophoresis is solely dependent on

field gradients. However, ∇E^2 states that dielectrophoresis is dependent on both field strength and gradients. Higher applied voltages lead to higher field magnitudes which lead to larger changes in field gradients.

One phenomenon which occurs at low frequencies is the formation of an ionic bilayer caused by the buildup of ions or polar molecules at the electrode surface. This layer serves as capacitive impedance against the applied voltage and reduces the effective field intensity [6,52-53]. Like a capacitor, the layer can be bypassed by operating at frequencies higher than the relaxation time constant of the medium $\tau = \varepsilon/\sigma$ [53].

2.4.1. Dielectrophoretic Manipulation of a Nanowire

Using the geometrical approximation of a prolate ellipsoid, the behavior of a nanowire with respect to the applied force differs depending on the rotational axis. As described by Jones, the relationship is described to be [50]:

$$F_{DEP} = \frac{2\pi r^2}{3}\left(\frac{l}{2}\right)\left[\frac{\varepsilon_2 - \varepsilon_1}{1+\left(\frac{\varepsilon_2-\varepsilon_1}{\varepsilon_1}\right)L_{\parallel}}\right]\frac{\partial E_z^2}{\partial z} \qquad \ldots(5)$$

$$T^e \approx \frac{4\pi r^2}{3}\left(\frac{l}{2}\right)\varepsilon_1 E_{\parallel} E_{\perp} \frac{(\varepsilon_2-\varepsilon_1)^2}{[\varepsilon_1+(\varepsilon_2-\varepsilon_1)L_{\parallel}](\varepsilon_2+\varepsilon_1)} \qquad \ldots(6)$$

where $L_{\parallel} = [1+\frac{3}{5}(1-\gamma^{-2})+\frac{3}{7}(1-\gamma^{-2})^2+\ldots]/(3\gamma^{-2})$, $\gamma = l/2r$, l and r are the length and radius of the nanowire respectively, and $\parallel$ and $\perp$ are the longitudinal and perpendicular

axis respectively. As before, all instances of permittivity have both real and complex components $\varepsilon + j\sigma/\omega$.

The electrorotation caused by dielectrophoresis is unique for this geometry. Similar to how spherical particles undergo positive to negative dielectrophoretic force with increasing frequency, the nanowire will experience positive force on each of its axes before moving into the negative regime.

Numerical studies had also shown that the nanowire length must match the size of the gap between two electrodes in order to assemble correctly. According to Liu *et al*, the assembly gap must be between 85% to 100% of the nanowire's length [53]. This size specificity can also be used for other applications such as filtering of bacteria [54].

Dielectrophoresis had been used to assemble conductive particles across two electrodes. Chains of gold nanoparticles and nanorods were successfully assembled to create an electrical connection between two electrodes [55-56]. Boote and Evans produced a well-rounded work on the assembly parameters of gold nanowires [51]. Fan *et al* investigated the efficiencies of gold nanowire assembly and established a direct relationship between voltage and frequency to assembly speed and alignment [57]. Additional work was conducted by Hamers *et al* to investigate the electrical characteristics of gold nanowire assembly inside an ionic medium [58] Multiple groups corroborated the positive relationship between frequency and alignment through the bypass of the capacitive ionic bilayer [47,58-61,65]. Smith *et al* also accomplished major work in this field by developing capacitively coupled arrays for the assembly of gold nanowires [61]. The assembly of zinc oxide, silicon, and gallium nitride nanostructures have all been successfully demonstrated [58,62-66]. Additionally, dielectrophoresis was

shown to be compatible with VLSI processes, opening up a new avenue of circuit integration [28]. Extensive work was also done to investigate dielectrophoretic assembly of carbon nanotubes in both numerical and experimental studies [67-70]. However, a reoccurring problem with all dielectrophoretic assembly processes is the local heating of the nanowire since their maximum current tolerance is very low [51,62].

A nanowire gas sensor requires the assembly of a *single* nanowire between two electrodes. Single nanowire assembly can achieved through conductive nanowires by causing the voltage between the electrodes to drop drastically after assembly. The drop in voltage causes the electric field to drop as well, hence decreasing the dielectrophoretic force and terminating the process. However, the assembly of a non-conductive nanowire would not be self terminating and would lead to the assembly of additional nanowires. While human interaction can stop the assembly from progressing any further, the ideal process should be fully automated without external intervention.

3 Synthesis and Characterization of TiO_2/TiO_x Nanowires

3.1. Experimental Goals

A suitable synthesis technique for TiO_2 nanowires must be developed beforehand in order to move towards a nanowire gas sensing platform. The synthesis of TiO_2/TiO_x nanowires through PVD VLS methods remains relatively uncommon as the processes still remain unclear. The use of a thin oxide layer instead of a titanium support layer as previously reported is the major innovation of these experiments. The growth mechanism can thus be isolated towards VLS rather than the VS mechanism. Using an oxide layer has other less obvious advantages such as reducing costs and processing time.

3.2. Experimental Design

The experiments were carried out using a 10cm diameter quartz tube inside a Lindberg Blue/M STF55346C 3-Zone RF furnace capable of reaching a maximum temperature of 1100 °C. The inert environment was created through the influx of Ar or a 5% Ar/O_2 gas mixture. The gas flow was fed into the system through approximately 3 m of 0.25" carbon steel tubing. The cylinder regulator used was a Praxair 109 Regulator and the flow rate was controlled near the furnace with a Praxair 65 mm variable area (series 65) flowmeter. Successful experiments were performed with a flow rate of 100 sccm or lower at pressures of 5 psi or lower.

A titanium source of 100 mesh powder was chosen to be the evaporation source to supply the metallic vapors. Approximately 1.5 g of titanium powder was placed in a ceramic boat at the center T2 of the furnace (Fig. 3).

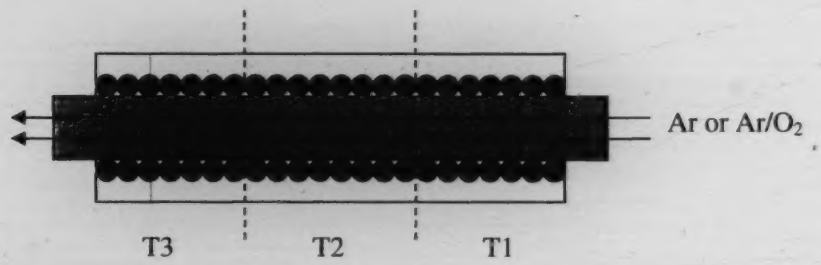

Figure 3: A general diagram of the experimental setup.

A quartz tube is inserted into the three-zone RF furnace, into which Ar or Ar/O_2 is flowed. The sample and source boat are placed in the middle T2 temperature zone.

Silicon substrates thinly-oxidized to 65-120 nm were used successful experiments. Gold was used as the catalyst of choice in order to provide a good basis of comparison towards existing work and because of its binary phase interactions with

titanium [44]. A custom sputter recipe with a forward power of 25 W and high spin speed for 20-40 seconds was used to deposit ultra-thin layers of gold.

The effect of surface roughness was also investigated using surface abrasion. The first sample was gently abraded using the application of grit zero SiC sandpaper. The second sample was lightly scratched using a diamond-tip scribing pen. The last sample was left untouched. All wafers were then oxidized after their surface abrasion treatments.

The sample and source boat were initially loaded into the center of the tube furnace. The tube was then sealed and purged with >250 sccm of Ar for 5 min before reducing the flow rate to less than 100 sccm. Temperature was ramped up to the reacting temperature in 2.5-3 h under an inert environment to prevent premature oxidation of the source material. The temperature was then was held for an hour under an Ar/O_2 environment. Afterwards, the temperature was ramped down for 2.5-3 h under Ar until room temperature was reached.

Scanning Electron Microscopy (SEM) was used after the growth process to confirm nanowire synthesis. X-Ray Diffraction (XRD) determined the lattice structure of the material. X-ray Photoelectron Spectroscopy (XPS) further confirmed the presence of titanium, while Auger Electron Spectroscopy (AES) provided surface information of the nanowires. Transmission Electron Microscopy (TEM) provided higher resolution images and electron diffraction to confirm the lattice structure of the nanowires.

3.2. Experimental Results

3.2.1. Initial Optimization of Nanowire Growth Parameters

Several experiments were performed to optimize nanowire synthesis and were found to be contingent on temperature, flow rate, and substrate placement.

Temperature directly affected the titanium vapor pressure within the system and facilitated the melting of gold. The vapor pressure of titanium was only significant at temperatures above 927 °C at around 9.69×10^{-9} Pa [71]. At 1100 °C, the titanium vapor pressure was [72]:

$$\log P/Pa = 5.006 + A + BT^{-1} + C \log T$$
$$A = 11.925,\ B = -24991,\ C = -1.3376 \qquad \ldots(7)$$
$$P \approx 3.42 \times 10^{-6}\ Pa$$

This partial pressure was small compared to the background Ar pressure of 5 psi or 34 kPa, leading to significant scattering or dilution of the source vapors.

The required Au-Ti binary compound only formed at 1064 °C when gold transitioned into a liquid phase [44,73]. However, a reduction in particle size could significantly reduce its melting point. For example, a diameter of 2.5 nm could reduce the melt of the gold nanoparticle to less than 50% of its bulk value [36]. While previous experiments demonstrated that gold did form their own individual nanoparticles at moderate temperatures, SEM images indicated that they did not melt into liquid gold droplets. Instead, they formed tetrahedronal/trianglar shapes possibly due to their relatively large size and thermodynamic forces [74-75]. Therefore, the reaction temperature was required to be at the melting point or higher to facilitate liquid gold droplet formation.

The flow rate of Ar/O_2 was kept at 100 sccm and lower to provide sufficient O_2 for titanium oxidation but not high enough to carry the source vapors away from the substrate. High flow rates were found to greatly suppress nanowire growth.

The sample was placed on top of the crucible in an inverted position similar to experiments performed by Lee *et al* and Zhang *et al* [12,46]. Similar to a covered pot, the local vapor pressure of titanium underneath the sample increased as the vapors had limited room to escape.

The recipe was successful on a mechanical grade Si (111) wafer with 120 nm layer of oxide. A grayish-white patch of approximately 3-4 cm^2 in size was formed on top of the sample. The SEM images (Fig. 4) show large masses of nanowires approximately 80-100 nm in diameter. Nanowire density was so high that it was difficult to provide an accurate numerical assessment. No nanowires were grown on areas of exposed silicon and heavily decomposed oxide, confirming that the oxide support layer was suitable for nanowire growth.

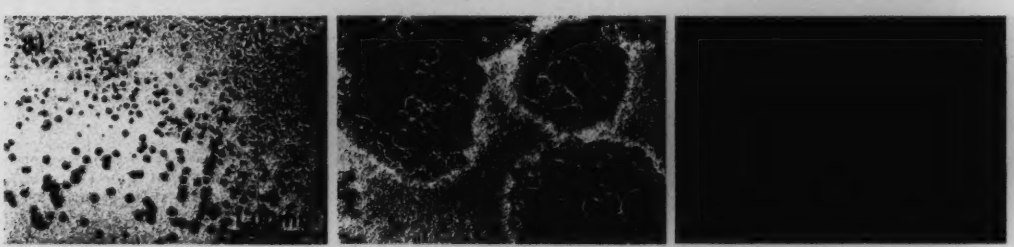

Figure 4: Successful nanowire growth using a mechanical grade wafer

From left to right: SEM images with increasing zoom on areas of nanowire growth. The nanowires are shown to be densely packed. Last scan c) indicates that the nanowire diameter is around 80-100 nm.

The nanowire's structure was revealed to be non-rutile TiO through XRD analysis (Fig. 5). Obtaining a relatively clear signal required a long scan time since the interaction volume of the XRD scan was large compared to the surface coverage of the nanowires.

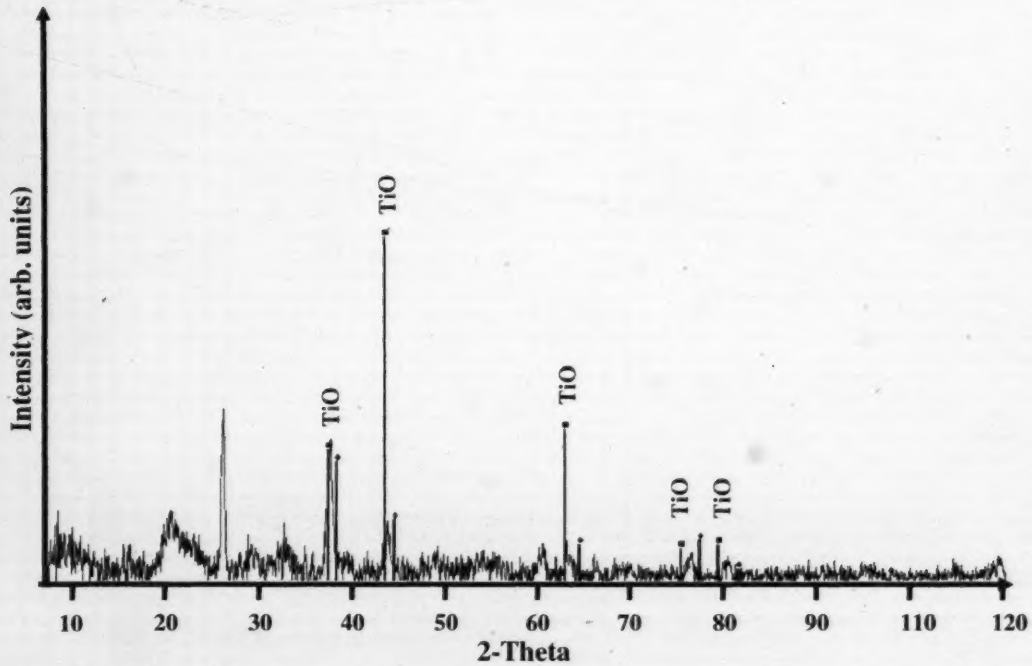

Figure 5: XRD Scan of mechanical grade wafer experiment

XRD scan of mechanical grade wafer experiment. TiO peaks were found as denoted by the red markers. No gold signal was found within the sample. Blue markers indicate the reference gold peaks.

Negative control experiments were performed on gold-deposited thickly oxidized samples to test for oxide dependence, and evaporated sapphire on silicon to test for the possible spontaneous VS formation of TiO_2 nanowires. No TiO nanowires were found, hence confirming the viability of the nanowire synthesis process.

3.2.2. Refinement Towards Rutile and Further Characterization

While the previous generation of nanowire synthesis was successful, defects and impurities cannot be easily controlled in a lower quality mechanical grade wafer. The recipe must move towards compatibility with a standard prime grade 110-orientation wafer to control for these factors. Furthermore, progression must be made towards rutile TiO_2 nanowires instead of the previously synthesized TiO since rutile structures required for gas sensing applications.

A prime grade wafer with 120 nm of oxide was used. The gold deposition was increased to 40 s to obtain a slightly thicker layer. Parameters for the rest of the experiment were left unchanged. The result was a mass of nanowires branching out in orthogonal lines approximately 2-3 nm thick across the substrate. The nanowires produced were of similar dimensions to the mechanical grade sample. However, the density was decreased as evidenced by the SEM images (Fig. 6).

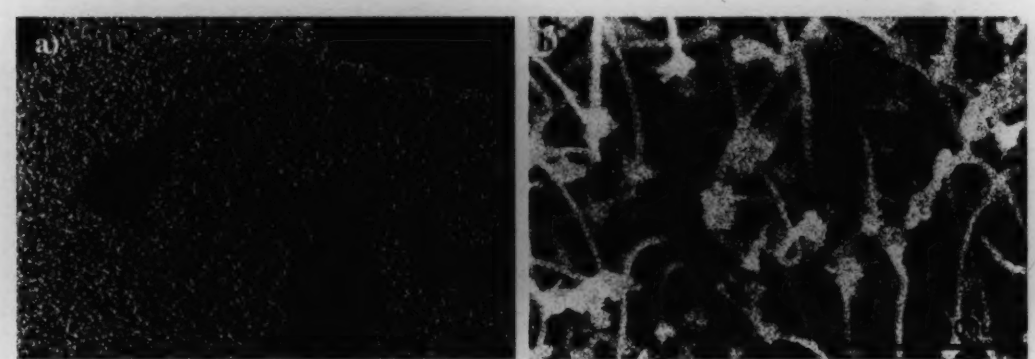

Figure 6: Successful nanowire growth using prime grade wafer.

a) A zoomed out view of the nanowire mass. b) Zoomed in image of nanowires. The nanowire patches are noticeably less dense as compared to previous experiments. Additionally, nuclei are clearly visible.

Negative control experiments, performed on gold-deposited non-oxidized silicon and thin oxide without any gold, produced no nanowires.

Further XRD analysis (Fig. 8) revealed the synthesis of rutile TiO_2 nanowires as opposed to the TiO nanowires previously obtained. Little to no change was made to the process parameters aside from the increased gold deposition and wafer quality, both of which should have no effect on oxygen content. The difference in oxygen content could therefore be due to a slight error in adjusting the flow rate and/or the gas pressure from the regulator. A glancing angle XRD scan helped confirm the weak rutile signals of the extended scan by producing significantly larger peaks. The resultant peaks were slightly shifted as expected but still correlated well with the reference rutile peaks.

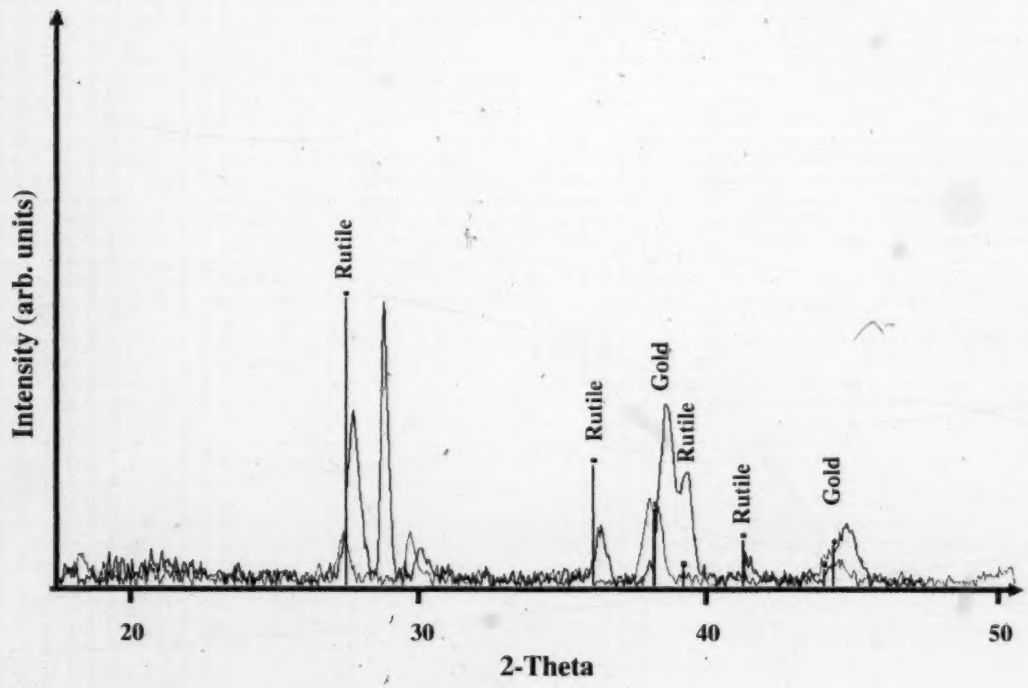

Figure 7: XRD scan of prime grade wafer experiment

The XRD scan reveals rutile TiO_2 and gold on the surface of the sample. Glancing angle scans, denoted by the black scan line, reveal additional rutile peaks to confirm its presence.

Elemental composition analysis was characterized by XPS and AES to further confirm the presence of titanium (Fig. 9). A weak titanium signal was revealed by XPS at approximately 462 eV despite good nanowire surface coverage. Similar titanium signals were found through AES by performing spot scans on the surface of the nanowire. Interestingly, AES also revealed the presence of a strong amorphous non-stoichiometric silicon oxide signal on the nanowire surface. Since AES is a surface characterization tool, a layer of amorphous silicon oxide was thought to be on the surface of the nanowire. This hypothesis corresponds well to the previous XRD data as an amorphous layer would not influence the data.

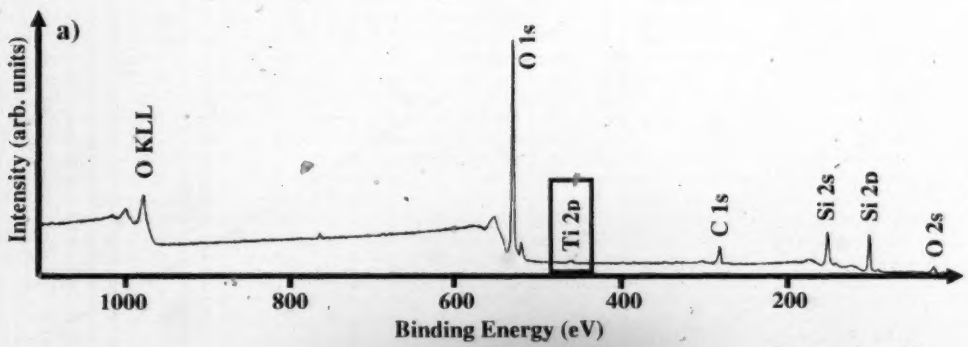

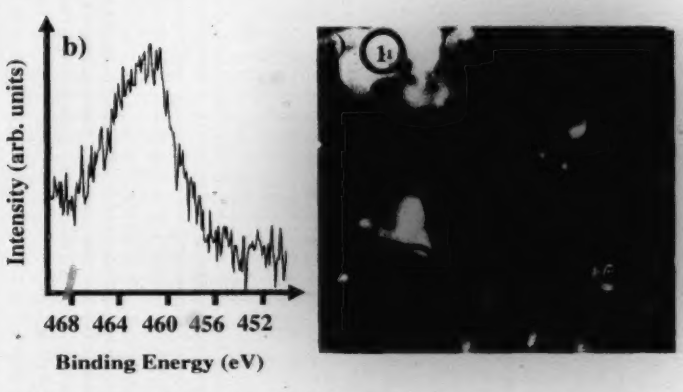

Composition (%)

	O	Si	C	Ti
#1	52.4	39.5	6.9	1.2
#2	42.4	49.6	6.4	1.6
#3	35	59.2	5.2	0.7
#4	53.2	39.8	7	0
#5	50.8	41.2	6	2
#6	51.6	30.1	14.9	3.4
#7	50.8	41.2	6	2

Figure 8: Surface characterization of prime grade wafer experiment

a,b) XPS data confirming the presence of titanium at 462 eV. c) AES data showing predominantly non-stoichiometric Si_xO_y on nanowire structures. A weak titanium signal is also found from the nanowires.

3.2.3. Improvement of Yield

Despite the relatively high yield, the amount of nanowires was still too small compared to the XRD interaction volume in order to generate a clear signal. Further characterization through TEM and any future sensor integration steps would be hindered as well, since small amounts of solution would rapidly dilute the dispersed nanowires. Therefore, the growth process must be optimized for high yields to allow for better characterization. Several experiments were performed to focus on the effect of oxide thickness, surface abrasion, and gas pressure on yield.

Oxide thickness: Two samples were prepared with oxide thicknesses of 200 nm and 65 nm respectively. The 200 nm oxide sample (Fig. 9a), using a slightly longer 60 second gold deposition time, did not produce any significant amount of nanowires. However, a possible VS growth pathway was demonstrated as scattered areas did exhibit hillocked growth of nanowires. The 65nm oxide sample, performed at 1.5-2.5 psi as reflected later, showed a dramatic increase in nanowire growth as the nanowire coverage extended along the entire titanium vapor-exposed surface.

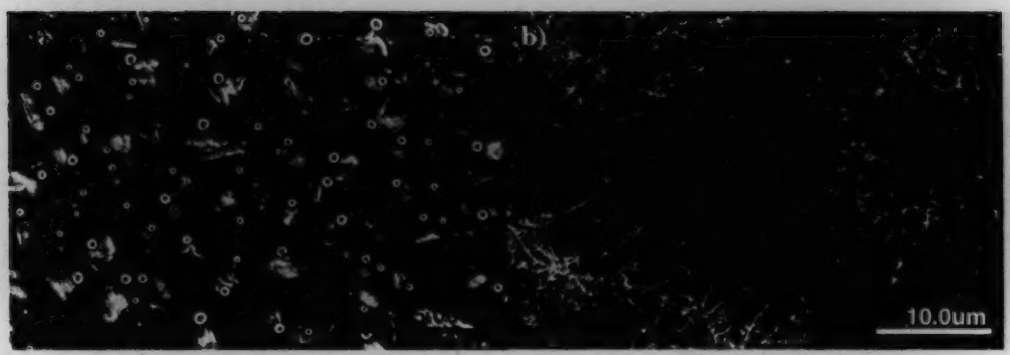

Figure 9: Effect of oxide thickness

a) 200 nm oxide sample exhibiting hillocked growth of nanowires. b) 65 nm oxide showing dramatic increase in nanowire coverage.

Surface Abrasion: No variance in nanowire growth could be observed with different surface abrasion treatments and identical oxide thicknesses of approximately 65 nm, especially between sandpapered and prime wafer samples of near-identical oxide thicknesses (Fig. 10). In fact, VLS nanowire growth seemed to *ignore* surface abrasion altogether as evidenced by nanowires growing over a mechanical scratch. The lack of effect could be due to the high reaction that dominates any benefit surface abrasion could have offered. Another possibility is that the surface was smoothed by the oxidation process and limited the effects of surface abrasion.

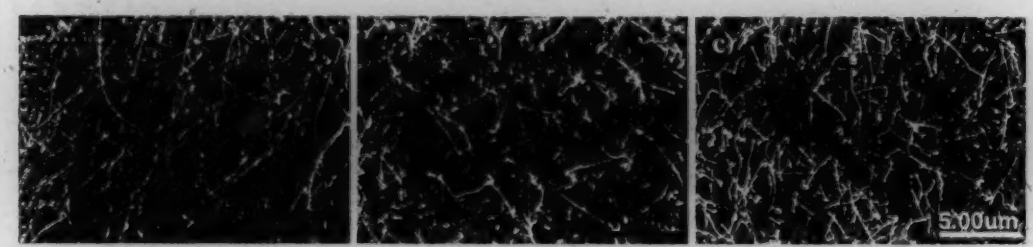

Figure 10: Effect of surface roughness with a 65 nm oxide layer

Left to right: Prime wafer to sandpaper treatment to mechanical scratching. All three wafers seem to show no substantial difference in growth density. c) Nanowires grow over a trench, as indicated by the dashed line.

Gas Pressure: Pressures were adjusted from the regulator to 10, 7, 3.5, and ~2.5-1.5 psi in separate experiments. The images indicated that higher pressures tended to produce more chaotic nanostructures. At 10 psi, protrusions grew from the nanowire surface, indicating that a high number of defects may have existed on the surface. At 7 psi, the nanowires were visibly jagged. Decreasing pressures correlated with higher orders of quality, with pressures of 3.5 psi and lower having no significant difference. Furthermore, XRD scans and TEM electron diffraction analysis done on the 2.5 psi sample indicated that the oxygen content was dramatically lowered and reverted back to the TiO lattice structure of previous recipes (Fig. 12 and 13). The two rings (Fig. 13) corresponded to the (111) and (311) faces of TiO instead of the expected (111) and (200) faces as indicated by the XRD scan. However, since the XRD (200) face is quite small, it is possible that a peak corresponding to the (311) phase exists at much higher angles. Additionally, the ring-like diffraction pattern indicated a poly-crystalline rather than a single crystal structure.

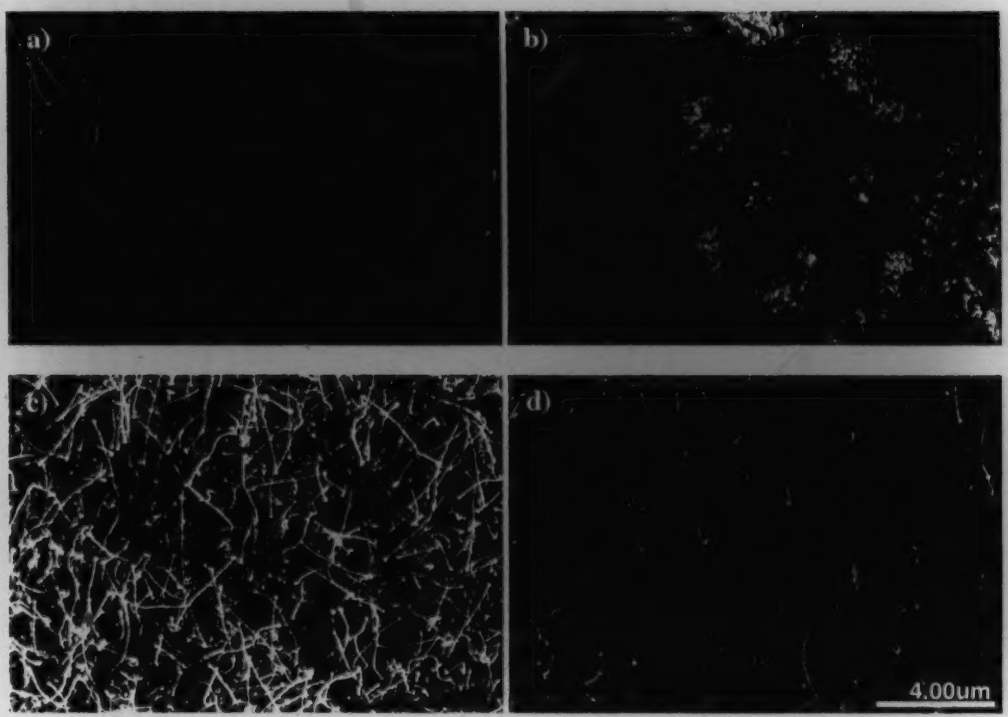

Figure 11: Effect of influx pressure

From top left to bottom right: a) 10psi, b) 7psi, c) 3.5psi, and d) 2.5-1.5psi. At high pressure (a-b), the nanowire structures are shown to be highly irregular and jagged. Nanowires grown at 3.5 psi and lower (c-d) exhibit relatively improved straightness and quality.

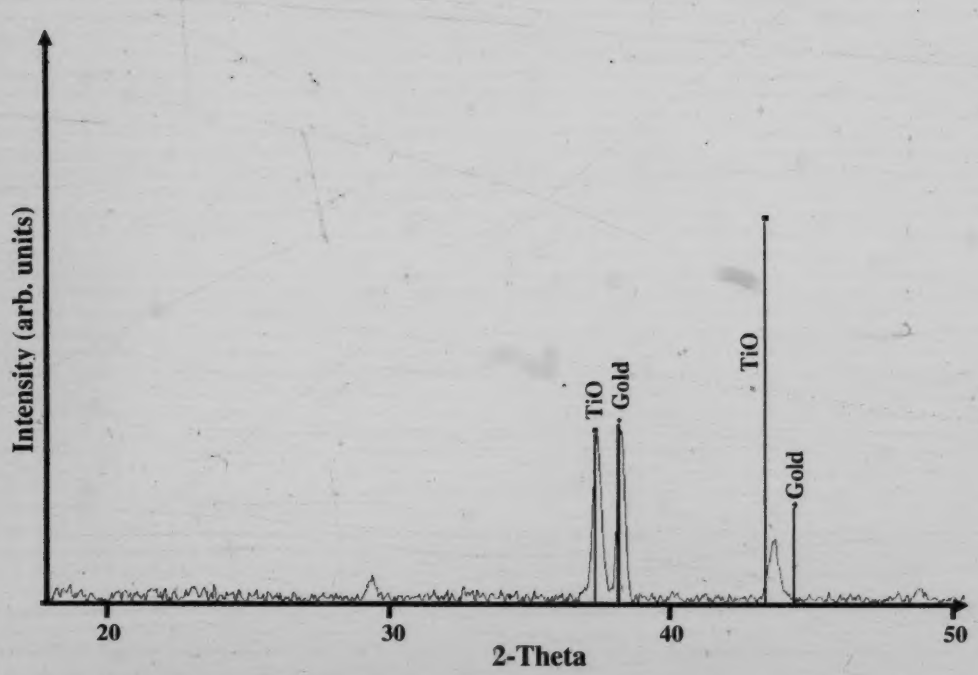

Figure 12: XRD scan of 65nm oxide sample

XRD scan shows two peaks corresponding with TiO and one peak corresponding to gold.

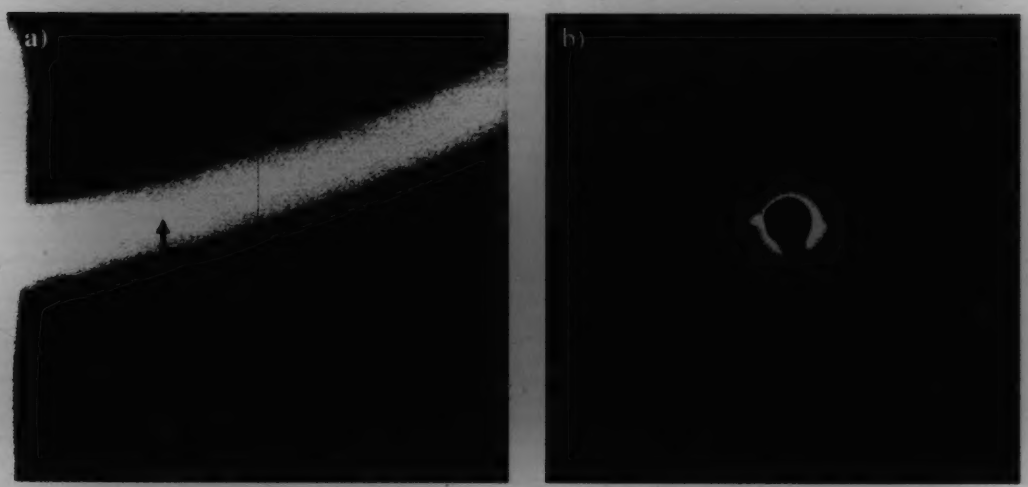

Figure 13: TEM image and electron diffraction analysis

a) Inner TiO core surrounded by amorphous Si_xO_y shell. b) Two polycrystalline rings corresponding to the (111) and (311) faces of TiO.

For completeness, Scanning Transmission Electron Microscopy (STEM) images were taken and gave direct evidence of VLS nanowire growth. The images (Fig. 15) revealed a circle of a different contrast within the nanowire's nucleus, which indicated that the spherical particle within was gold.

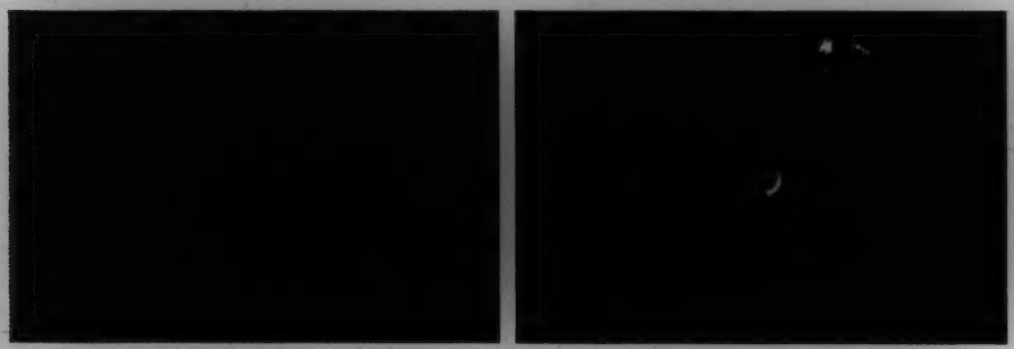

Figure 14: STEM images of nanowire and nucleus

a) STEM image of nanowire growth with a dark circle inside the nucleus, which indicates a gold nanoparticle. b) SEM image of the same nanowire and nucleus.

3.3. Discussion of Results

The previous results and negative controls demonstrated that the VLS growth mechanism is responsible for TiO_2/TiO_x nanowire synthesis in this setup. However, the role of the thin oxide is still unclear as its effect seems to be thickness dependent. Studies had shown that thin silicon oxide layers will decompose at high temperatures in an inert or vacuum environment by undergoing the following reaction [37-38,76-78]:

$$Si_{(s)} + SiO_{2(s)} \xrightarrow{inert} 2SiO_{(g)} \qquad \ldots (8)$$

The breakdown of thinner oxides near the growth sites (Fig. 15) suggests that some kind of decomposition effect aids the growth of nanowires. The hypothesis is that the decomposition of Si and SiO_2 releases SiO, which redeposits onto the oxide layer and

results in the creation of a vitreous metastable layer of amorphous oxide [38]. Gold is then more readily able to coalesce on top of this metastable layer, which aids in the growth of a nanowire. Since this reaction is an interfacial reaction, a thicker oxide would prevent its upward diffusion while a thinner layer would allow the SiO species to diffuse through [37]. While this process can result in amorphous Si_xO_y nanowires, a thin oxide layer may be enough to suppress their growth while simultaneously allowing for the formation of the metastable layer. Further evidence for the presence of SiO can be found with the amorphous Si_xO_y sheath, as any excess SiO would crystallize on the nanowire.

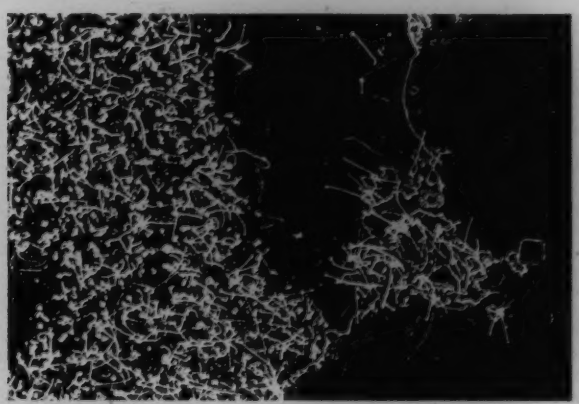

Figure 15: Decomposition of thin oxides

Nanowires are shown to grow on the darkened partially decomposed oxide area, whereas it does not grow on the heavily decomposed oxide surface to the right.

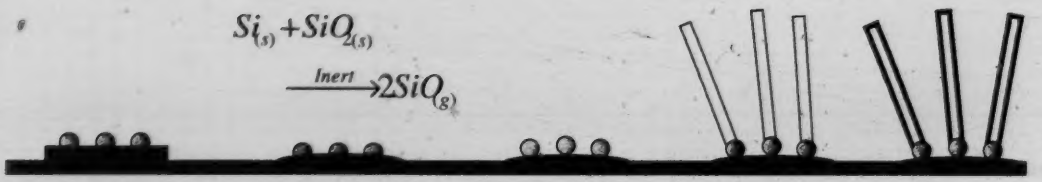

Figure 16: Illustration of the proposed growth process.

Gold film initially undergoes island formation and forms individual solid particles. The thin layer of oxide reacts with Si in high temperature inert environment, and decomposes into vitreous metastable layer. Subsequently, the gold particles melt into liquid droplets and coalesces on top of the Si_xO_y layer. Nanowire formation results from these liquid droplets, which are then covered by Si_xO_y due to any excess SiO in the system.

Some degree of composition did occur with thicker oxides as evidenced by dark circular patterns on the surface (Fig. 16a). High quality crystalline nanowire growth did occur in these spots (Fig 16c), but was rare and cannot be consistently produced. Additionally, these nanostructures seemed to show a higher degree of crystallinity compared to previous samples, but their composition could not be determined as their quantity is too small. Despite the low yield, the oxide layer was still highly active and demonstrated that nanowire growth continued to be possible even with increasing oxide thickness.

Figure 17: Decomposition of thick oxides

From left to right: Decompositional effect of thicker oxide layers. Some type of nanowire structure is present, but their growth is limited.

3.4. Summary

Two distinct types of titanium-based nanowires with amorphous Si_xO_y sheaths were synthesized on a thin layer of oxide through the VLS growth mechanism. Control between TiO_2 and TiO formation was done by controlling the influx pressure of Ar/O_2. Elemental compositional analysis was performed through XPS and AES and the crystal structure was confirmed through XRD and TEM. A direct relationship between oxide thickness and nanowire growth was found, as a thinner layer seemed to mediate nanowire growth by forming a metastable layer of oxide. Surface abrasion had no effect on nanowire growth, either due to the high temperature process or a smoothening effect due to the thermal oxide growth step.

4 Dielectrophoretic Assembly of Nanowires

4.1. Experimental Goals

Dielectrophoresis offers the ability to assemble multiple nanowires over many electrodes rapidly and efficiently. Furthermore, dielectrophoresis enables top-down design approaches by assembling nanowires over *existing* electrodes rather fabricating electrodes *on top* of individual nanowires. A single nanowire is favorable for nanowire gas sensors as multiple resistive elements in either parallel or series would decrease the overall sensitivity of the device. This chapter will focus on the experimental setup and design of the dielectrophoretic process. Following that will be an exploration of optimal parameters in the assembly of different nanowire materials.

4.2. Types of Nanowires

Attempts at dielectrophoretic assembly of other nanowire materials concurrently occurred with TiO_2/TiO_x nanowire synthesis to provide a basis for their future assembly. The nanowires thus attempted were gold and zinc oxide (ZnO) nanowires.

Gold nanowires synthesized by templated electroplating were provided by Brian Edwards of University of Pennsylvania using a process first developed by the Moskovits, Martin, and Mallouk groups [79-81]. The nanowires were suspended in DI water and had to be diluted before use. They were found to be approximately 4-6 μm in length and 200 nm in diameter (Fig. 17). Many nanowires showed rough edges and branching along the ends, but ultimately did not interfere with the dielectrophoretic process.

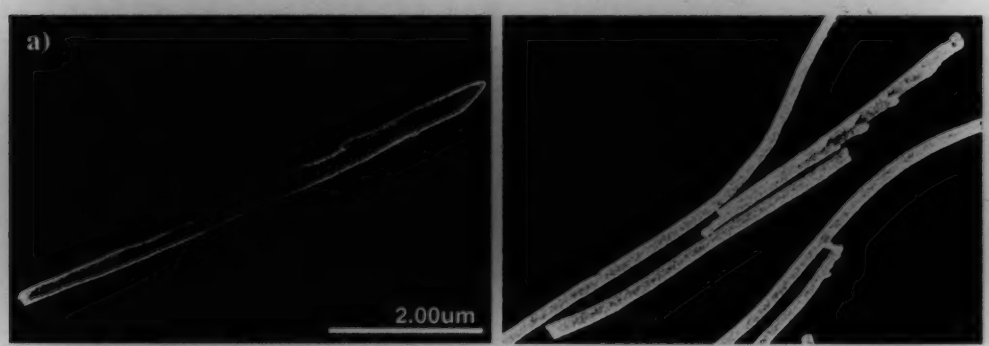

Figure 18: Gold nanowires synthesized through template electroplating

The gold nanowires supposed by University of Pennsylvania were shown to have a diameter of approximately 200 nm and a length of 4-6 μm. Rough edges can be seen on the edges of the nanowires.

The ZnO nanowires were provided by Dr. Jyh-Ming Ting of the National Cheng Kung University of Taiwan [82]. These single crystal nanowires were grown by a RF sputtering process and were observed to be approximately 200 nm in diameter with most lengths restricted to 2-4 μm (Fig. 18). The nanowires were initially suspended in ethanol and had to be transferred to DI water before use. Additionally, many of the zinc oxide

nanowires tended to aggregate (Fig. 18b). Whether this was due to the existence of a polar face on the nanowire or the growth methods was unknown. In any case, nanowire aggregatation was solved by placing the solution into a sonication bath prior to nanowire assembly.

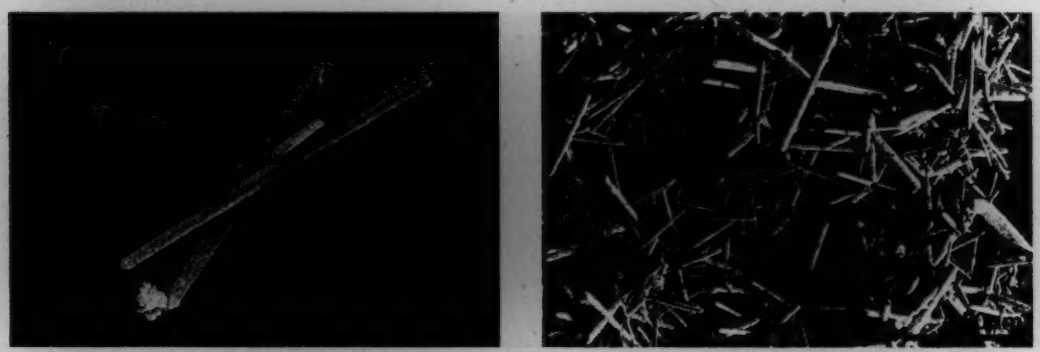

Figure 19: ZnO oxide nanowires synthesized by PVD methods

ZnO nanowires provided by Dr. Jyh-Ming Ting of the National Cheng Kung University of Taiwan. Thicknesses were again approximately 200 nm in diameter with a variety of lengths, mostly in the 2 μm range. The nanowires tended to clump up with each other, as seen on the right.

4.3. Experimental Design

The experiment was performed by adding a drop of sonication-dispersed nanowire-suspended DI water solution on top of an electrode array. Voltages ranging from 10-35 V_{pp} were applied through the electrodes for about a minute or until visual confirmation of nanowire assembly is found. The solution and voltage were then removed and optically inspected for confirmation of assembly (Fig. 19).

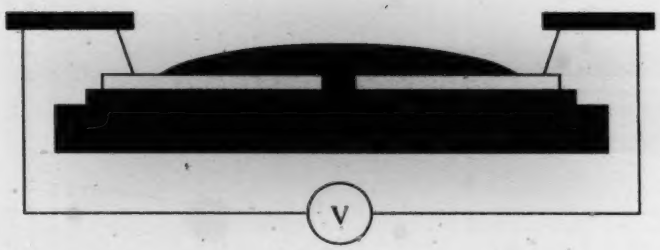

Figure 20: Dielectrophoretic assembly process

A drop of nanowire solution is placed on top of the electrode array, shown in yellow. Probers are used to make electrical contact with the electrodes, through which voltage is applied.

The experiments were conducted at two separate facilities. The first iteration of the work was performed inside the 10k area of the University of Alberta Nanofabrication facility (Nanofab), while the second took place inside the 10k area at the National Institute of Nanotechnology (NINT). The 10k area of the Nanofab was equipped with a Wentworth Probe Station with four manual probers. A BK Precision 4017A function generator was used to provide the necessary voltage and frequencies. The 10k area of NINT was equipped with an Ultracision Inc 680E Semi-Automatic wafer prober. A Leica GZ7 stereoscope and four manual probers were attached. Voltages and frequencies were supplied from a HP 3245a Universal Source equipped with a 10x voltage booster current limited to 100 mA.

Various electrode designs were used in the course of these experiments. Each experimental section will highlight and discuss the electrode design(s) used.

4.4.1. Iteration 1: Nanowire Assembly Under Vibrational Environments

The first round of experiments focused on developing an overall theory and technique in the design and construction of the assembly electrodes. Based off previous work at Virginia Tech [28], the design provided a pair of thin finger-like electrodes for a nanowire to assemble between, and capacitive coupling between multiple electrodes to actuate them all simultaneously.

A three mask-layer approach was used to create a buried electrode layer, a dielectric layer, and a top electrode layer. The top and buried electrodes through the dielectric layer formed a capacitive link which passes the voltage to the top electrodes (Fig. 20). A capping layer to clamp down the nanowires after assembly would be ideal, but limitations such as keeping the nanowire in place during processing made it unfeasible.

The first and third electrode layers were composed of sputtered gold on top of SiO_2 and a chrome adhesion layer (Fig. 20b,f). The metallic layers were patterned, exposed, and developed using HPR 504 photoresist, four seconds of UV light, and aqueous 354 developer. KI/I gold etch and commercial chrome etch were used to remove the exposed metallic layer and define the electrodes (Fig. 20c,g). The buried electrode layer was approximately 250 nm thick while the top electrode layer was about 90 nm. The insulating dielectric layer was grown using plasma-enhanced chemical vapor deposition (PECVD) of a tri-ethyl oxy-silane precursor grown to approximately 250nm as verified by optical filmetric measurements (Fig. 20d). The VIA holes were defined with the above method, and etched with Buffered Oxide Etch (BOE) (Fig. 20e).

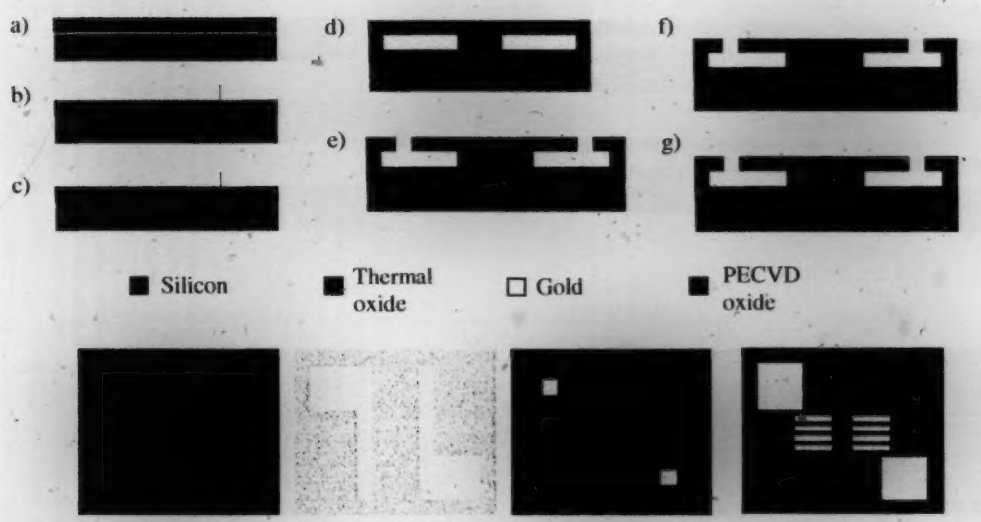

Figure 21: Process flow for the creation of dielectrophoretic assembly finger electrodes with capacitve coupling (Mask design 1)

A simplified process flow is described through these images. First, a bare wafer is oxidized (a), on top of which gold is deposited (b). The gold layer is then patterned and etched away (c-d) and covered with an insulating layer of PECVD oxide. The oxide is etched through and deposited again with gold to form VIAs to the bottom layer (e-f). The gold layer is patterened and etched again to form the finger electrodes on top (g). A short top-down view of the process is shown on the bottom set of images, showing one set of finger electrodes.

The assembly of gold nanowires was attempted by using a 1 mL drop of nanowire-suspended DI water solution and the application of 10 V_{pp} and 1 MHz. The assembly process occasionally worked and resulted in nanowires bridging the electrodes. However, most cases resulted in zero movement of the nanowires. Moreover, the nanowires would float away after assembly once the voltage was removed.

A lack of voltage through the coupling of several electrodes was suspected so a negative control was conducted by creating single sets of electrodes without capacitive coupling (Fig. 21a). As expected, nanowire assembly was successful with the identical application of 10 V_{pp} and 1 MHz. However, the nanowire and electrode melted after assembly (Fig. 21b), possibly due to exceeding the maximum current capacity of the

nanowire. A secondary negative control was performed with DI water to confirm the destruction was due to nanowire assembly (Fig. 21c).

a)

b)

c)

Figure 22: Single electrode pads with finger electrodes (Mask design 2)

a) The second mask design provided several electrode pads and finger electrodes without capacitive coupling. Optical images of: b) nanowire and electrode destruction after assembly, and c) no electrode damage with DI water as a negative control.

The first mask design experienced many process difficulties, such as alignment run-off due to surface stress and sensitivity to surface contamination during the PECVD process. A third single-layer process was made to overcome these obstacles (Fig. 22). The design offered large features enabling ease of use and processing, and pads allowing direct and capacitively-coupled assembly. Additionally, the design allowed the actuation of a *single* electrode with a capacitive link to block high amounts of current, which was not possible with the previous design.

Figure 23: Single layer assembly electrodes (Mask design 3)

This versatile mask allowed a variety of parameters to be tested. Assembly pads on each side of the finger electrodes allow direct actuation to be tested. Comb tooth capacitors on both sides serves as current blocks and only needs one manual prober to be moved between each successive assembly. Inlet shows triangular pads tapering off into a set of finger electrodes.

Using this new mask, assembly was possible with the actuation of a single electrode with a capacitive gap using 10 V_{pp} and 1 MHz. However, the nanowire still did not stay assembled and floated away soon after the voltage was removed (Fig. 23). Sequential images with no voltage applied were taken and found substantial movement of nanowires under solution (Fig. 24). Mechanical vibrations were suspected to be the cause as the Nanofab 10k area contained several sources of vibrational noise.

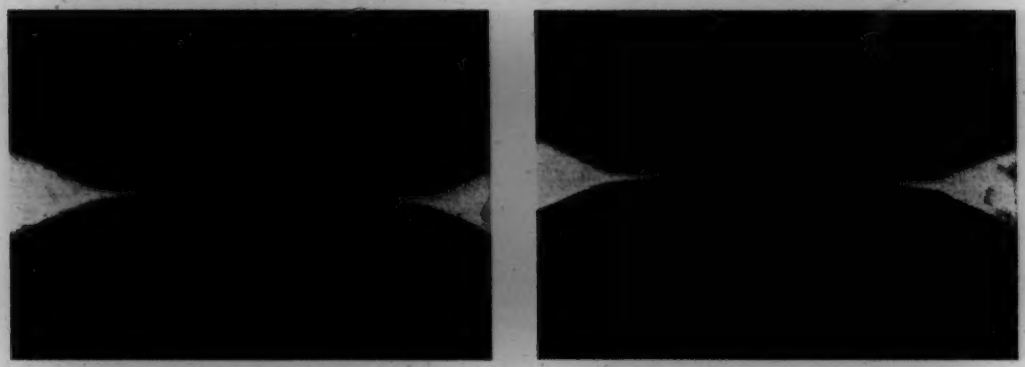

Figure 24: Nanowire assembly with third mask

a) Nanowire assembly was successful with the third mask. b) Nanowire dissembles from the electrode after removal of voltage.

Figure 25: Vibrational effects on a gold nanowire solution

Consecutive optical images taken of the assembly electrodes with no voltage applied. Circles highlight the most visible nanowire movement.

4.4.2. Iteration 2: Nanowire Assembly Under Quiet Environments

A drastic measure was taken to mitigate vibrational noise by moving the entire process to the NINT 10k area. The HP 3245a universal source was used to supply higher voltages. A slight tweak to the assembly process was also made by using a cleanroom wipe to absorb the nanowire droplet after assembly had been completed.

Nanowire assembly was successful with the consistent assembly of nanowires across electrodes and remained in place after the removal of the solution and voltage.

Surprisingly, single nanowire assembly was successful under lower voltages and frequencies rather than higher ones. At one extreme, 35 V_{pp} and 1 MHz resulted in multiple nanowires disorderedly assembled across a gap (Fig. 25). Conversely, highly aligned single nanowire assembly was achieved at 15-25 V_{pp} and 250 kHz (Fig. 26a,b). The assembly process seemed to be more *ordered* with decreased dielectrophoretic force and resulted in fewer assembled nanowires over a single site. However, there was a threshold for viable assembly as no nanowire assembly was seen below 15 V_{pp}. This difference in voltage compared to the Nanofab setup was likely due to different impedance matching between both probe stations and source generators.

Figure 26: Assembly of nanowires at 35 V_{pp} and 1 MHz

Nanowire assembly is successful for these parameters, but the result is disordered with more than one nanowire bridging the electrode gap.

Optical confirmation of nanowire assembly was verified by SEM images (Fig. 26c,d). Partial assembly of nanowires was also found, resulting in a small gap between the assembly electrode and the nanowire. This observation agrees with studies, as nanowires would favorably assemble if the nanowire and electrode gap sizes are comparable to each other [53].

Figure 27: Single nanowire assembly of gold nanowires

Single gold nanowires are assembled over electrode gaps. a,c) 15 V_{pp} and 250 kHz. b,d) 25 V_{pp} and 250 kHz.

4.4.3. Iteration 3: Assembly of ZnO Nanowires

A fourth mask design was created to facilitate the assembly of the ZnO nanowires. The electrode gaps were made smaller as were the electrode widths. Fifteen assembly sites in total were made compared to the previous five. Capacitive coupling was also possible from both sides of the electrodes. However, process difficulties with lithography and UV over-exposure of photoresist (Fig. 27) pushed the assembly process back to the third design.

a)

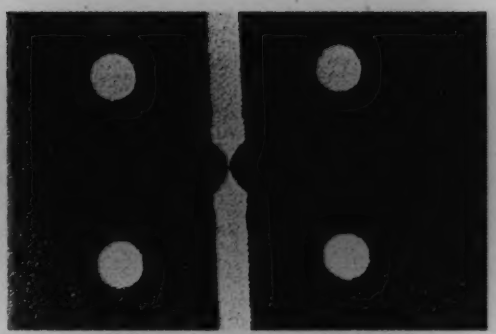

Figure 28: Overview of second-generation single layer assembly electrodes (Mask Design 4)

Long electrode lines extended from the contact pads, which were coupled together through another electrode gap. However, process difficulties concerning exposure and lithography made this design untenable for long-term use.

The assembly of ZnO nanowires was met with some potential challenges. The semiconductive nature of ZnO nanowires would make a self-terminating process impossible. Additionally, the ZnO nanowires were initially suspended in methanol instead of DI water and did not remain as a droplet when applied to an oxide or nitride surface. Replacing methanol with DI water resulted in the formation of nanowire clumps and required significant amounts of sonication over gold nanowires. The dispersion lasted only for a short period of time and led to an overly time-consuming process.

Nanowire assembly was obtained at 25-35 V_{pp} and 100-250 kHz, but as expected, multiple nanowires bridged the electrode gaps instead of single nanowires (Fig. 28). Leaving the voltage on was not a viable option as the dielectrophoretic force combined

with eddy effects would draw excessive numbers of nanowires to the site. Leaving the voltage off would result in the detachment of the nanowire from the electrode surface when the drop meniscus passed over the nanowire during the droplet removal. Moreover, near-identical parameters did not show consistent results with consecutive experiments as spontaneous clumping made single nanowires unavailable.

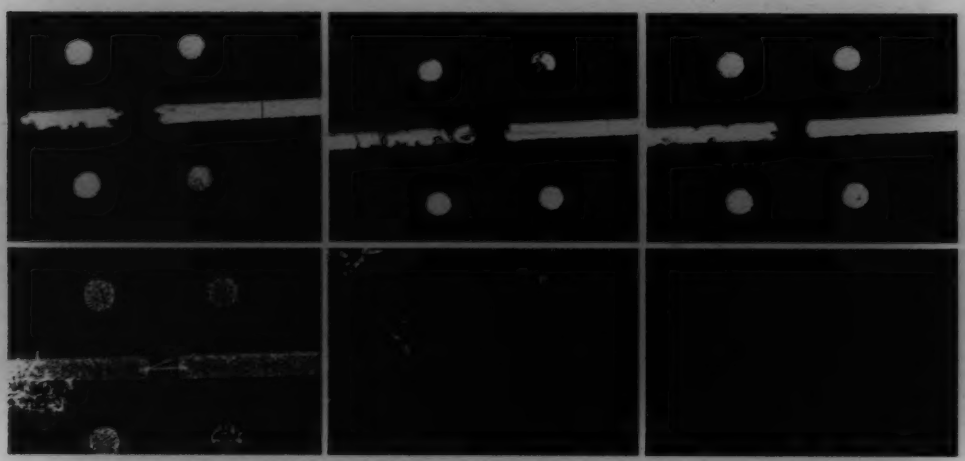

Figure 29: Dielectrophoretic assembly of ZnO nanowires

From left to right: a,d) 35 V_{pp} 100 kHz, b,e) 35 V_{pp} 250 kHz, c,f) 25 V_{pp} 250 kHz. Optical images reveal several nanowires assembled across each gap, confirmed by SEM images. Strangely, while the last set showed something in the optical image, nothing was revealed under SEM. Some nanowires seem to be missing from the SEM images as well.

Strangely, the pull-off speed for the solution droplet was slower for this round of experiments than previously done and often left a thin film of solution on the surface. While it was initially theorized to be due to trace amounts of methanol, later DI water-only nanowire solutions did not see an improvement. Switching the base layer from oxide to nitride had no significant effect. The only probable cause left was that the cleanroom wipes used in the initial round of experiments were different than the later ones, which would account for the difference in absorbancy rates.

4.5. Discussion of Results

While literature had stated that higher voltages and frequencies generally aid the assembly process for both conductive and non-conductive nanowires [52,57,60-61,65], it had not been the case for our current experiments. Contrary to expectations, a *lower* dielectrophoretic force for both nanowire materials helped the assembly process. The proposed hypothesis suggested that smaller forces allowed for a less chaotic assembly process and thus allowed for the assembly of a single nanowire. While lower voltages did guarantee lower DEP forces, the effect of frequency remained unclear. From a qualitative point of view, decreased frequency should generate a higher dielectrophoretic force. On the other hand, increased frequency should also produce better alignment regardless of conductivity of the nanowire, as already stated. None of these effects were observed over the course of experimentation. Therefore, a formal numerical analysis needs to be performed to further explore the effect of frequency.

Other frequency-related issues still remain, such as the relationship between high frequency operation and local heating effects. Previous work had stated that higher frequencies correlate to a decrease in local heating effects [51,62]. However, the application of a 10 V_{pp} and 1 MHz signal still caused the nanowire to melt. A theoretical analysis must be performed to explain this discrepancy.

4.5.1. Dielectrophoresis and Electrorotation

Alignment forces can be quantified by examining the electrorotational equations due to dielectrophoretic force. The earlier equation (Equation 6) for the prolate ellipsoid can be further generalized as [50]:

$$\langle T^e \rangle_\alpha = \frac{2}{3}\pi\left(\frac{l}{2}\right)r^2\varepsilon_1(L_\gamma - L_\beta)\mathrm{Re}[K_\beta K_\gamma] \qquad \ldots(9)$$

In this equation, β and γ represent the different axes of the nanowire with respect to the rotational field axis α. The equation can be simplified by assigning the nanowire's axis α to be on the same axis as the external electric field, hence turning β and γ into perpendicular and parallel components. The frequency contributions can now be evaluated by examining the K_β and K_γ components [50]:

$$K_\beta \equiv \frac{\varepsilon_2 - \varepsilon_1}{3[\varepsilon_1 + (\varepsilon_2 - \varepsilon_1)L_\beta]} \qquad \ldots(10)$$

Each of the permittivity terms can be expanded to include the complex conductivity components. A τ_{MW} term similar to earlier approximations can then be extracted out of this equation:

$$\tau_{MW,\beta} = \frac{(1 - L_\beta)\varepsilon_1 + L_\beta\varepsilon_2}{(1 - L_\beta)\sigma_1 + L_\beta\sigma_2} \qquad \ldots(11)$$

The significance of the τ_{MW} term here is that it defines the torque roll-off frequencies and hence the points where the nanowire begins to align itself to the other axis [50]. For instance, the nanowire would rotate from a parallel orientation to align itself perpendicularly to the field at $\tau_{MW,\parallel}$ as the torque rolled off, while the nanowire would again align itself to be parallel at $\tau_{MW,\perp}$.

By doing some simple calculations, ε_1 and σ_1 being $78.36\varepsilon_0$ and 0.0550 μS/cm for DI water, and ε_2 and σ_2 being ε_0 and 45.45×10^6 S/m for gold [83-85], the result is $\tau_{MW} = 1.546 \times 10^{-17}$ s for the perpendicular case and corresponds to a frequency of 6.469×10^{16} Hz. A similar calculation can be made for the parallel case, leading to $\tau_{MW,\parallel} = 2.27 \times 10^{-15}$ s or 4.403×10^{14} Hz. While these calculations are for the general case where the DI water medium is completely pure, adding even a small conductivity component does not matter in this case as the term in dominated by the response time of the conductive nanowire.

The implication of these numbers is that the experimental frequencies for the gold nanowire assembly were nowhere near these limits. Furthermore, operation at MHz and lower frequencies forces the system to behave in the low-frequency regime dominated by the conductivity of the medium and the nanowire. No significant change from 100 kHz to 1 MHz can be observed since $\omega\tau_{MW}$ remains very small. This numerical analysis agrees with the assembly efficiency analysis done by Fan *et al*, where there was little difference between the two frequencies [57].

The analysis is slightly convoluted for ZnO. The first turnover frequency from parallel to perpendicular is approximately 9.688 kHz using the worst case scenario of 10 Ω/cm as the resistivity [86]. The next turnover frequency is substantially higher at 1.937 MHz. The ZnO must therefore be significantly doped since aligned assembly of multiple nanowires *was* observed in the 100 kHz range. The lack of frequency dependence also agrees with the gold nanowire model described above, suggesting that the assembly process is again held in the low-frequency regime.

The conclusion is that the nanowires experienced little to no effect due to the frequency range used during the course of experimentation. No significant benefit

towards nanowire alignment can be found within the frequency range of 100 kHz to 1 MHz. The process is instead dominated by the amount of voltage applied. Therefore, lowering the voltage would be the only feasible method in generating lower dielectrophoretic force.

4.5.2. Other Frequency Response Issues

The discrepancy between the results and literature with respect to heating issues can be explained through the formation of interfacial capacitance layers between the medium and electrode. An ionic double layer forms whenever a voltage is applied to an electrode and creates a virtual capacitance layer [52-53]. At low frequencies, this layer is insulative and prevents current from escaping the electrode. At higher frequencies, this layer can be a conductive path due to its capacitive nature. An increase in solution conductivity also makes this path more favorable for electric current [58]. Hamers *et al* had stated that this alternate conduction path can be as much as 1000x larger than the nano-ampere level current passing through the nanowire [58]. In other words, most of the current is passed through the nanowire at low frequencies whereas most of the current is passed through the solution at higher frequencies.

The benefits of higher frequencies cannot be seen in our own experiments because of the use of non-conductive DI water. The current held by the sink is determined by the solution's ionic content [58], thus making DI water a non-favorable conduction path. The use of methanol by Boote and Evans may have been conductive enough to sink enough current for their application of 2-3.5 V_{pp} and 150 kHz [51]. In our case, the use of DI

water was not enough to protect against 10 V_{pp} and 1 MHz. Therefore, a capacitive block is needed to prevent the draw of excess amounts of current into the nanowire.

4.5. Summary

Assembly of individual gold nanowires was successful with the application of 15-25 V_{pp} and 250 kHz. Supporting factors such as the mitigation of vibrational noise and improved electrode design contributed immensely to this achievement. Additionally, a smaller dielectrophoretic force was found to be favorable in the assembly of a single nanowire. The assembly results were confirmed through optical and SEM images. Assembly of ZnO nanowires were also attempted with partial success as multiple nanowires were assembled across the two electrodes. Improvements for future processes still need to be made, such as improving the consistency of ZnO assembly.

An analytical investigation into the effect of frequency was conducted and found that the experimental frequencies used had no significant effect on nanowire assembly. Additionally, higher frequencies were found to not protect against the local heating of nanowires contrary to reported data because of the differences in solution conductivity.

5 Conclusion

The successful growth of TiO_2/TiO_x nanowires and the single nanowire assembly of gold nanowires were completed. Nanowires composed of TiO_2 and TiO were successfully synthesized using the VLS growth mechanism and the absence of a titanium-based support layer. Yields were significantly improved during the course of experimentation. Elemental composition was confirmed through XPS and AES studies. Crystal analysis from XRD and TEM confirmed the nanowire's structure. Additionally, AES and TEM scans revealed an outer coating of amorphous Si_xO_y. Single gold nanowire assembly bridging two electrodes was achieved using dielectrophoresis. Experimental results revealed a direct dependence of the size of dielectrophoretic force and the number of nanowires assembled. Assembly results were verified through optical microscopy and SEM.

Both of these successes are significant milestones towards creating a nanowire gas sensing platform. Thermally grown TiO_2 nanowires through the VLS growth mechanism are still relatively uncommon and this study greatly contributes to the overall understanding of the growth process. The assembly of gold nanowires, while reported several times, provides a new set of parameters for use in the project's future.

There are several factors to consider for the future evolution of this project. Conductive nanowires must be used to create a reliable assembly process as demonstrated by the work done on the zinc oxide nanowires. The use of segmented nanowires whereby an inner region of semiconductive material is capped with conductive ends is one way around this problem. The dielectrophoretic force from the conductive portions dominates and forces the nanowire to assemble as if it was entirely conductive (Fig. 29). However, single nanowire assembly still requires the conductivity of the *entire* nanowire, which can be overcome by applying enough voltage to overcome the schottky barrier between the conductive and semiconductive segments. Associated group work with Y. Dan *et al* and the assembly of segmented gold and PEDOT/PSS nanowires has already been accomplished [32].

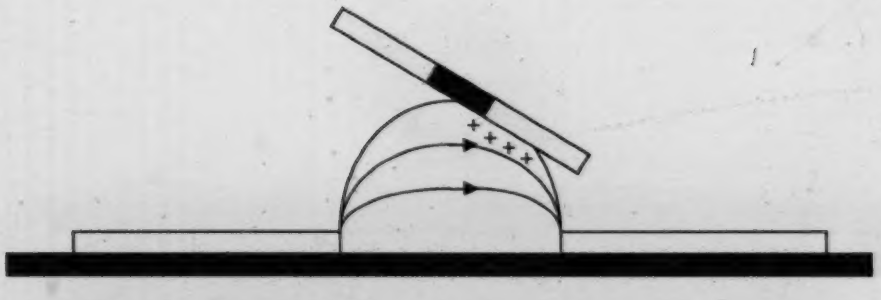

Figure 30: Dielectrophoretic assembly of a segmented nanowire

A segmented nanowire is assembled onto a pair of electrodes. The dielectrophoretic force exerted on the nanowire is dominated by the conductive segments of the nanowire rather than the central semiconductive region.

Coincidentally, TiO nanowires are a prime candidate for the assembly process due to its conductivity. However, the layer of amorphous Si_xO_y covering the nanowire may block any conductive effects. One solution is to directly remove the sheath by HF treatment. However, it is unknown whether HF would directly attack the TiO core. Another method is to use a non-silicon substrate such as sapphire or fused silica. However, the current process is optimized for the use of thin oxides and may not be compatible with other substrates. Furthermore, Lee *et al* demonstrated that the nanowire crystal quality is dependent on the substrate used [12]. Additional work will be needed to convert the process for different substrate materials.

Additionally, TiO_2 must be reemphasized as the gas-sensing material of choice. However, the semiconductive nature of TiO_2, like ZnO, makes it an unsuitable candidate for single nanowire assembly. A simple post-assembly heat treatment under oxygen can possibly force an assembled TiO nanowire to transistion into rutile TiO_2. The only complication with this process is the possible inter-diffusion of the chrome adhesion layer

and the gold electrode at elevated temperatures. This complication can be avoided simply by selecting a different adhesion layer or substrate.

One step that should have been perfomed post-assembly was the clamping of the nanowire to the electrode surface. Practical considerations limited the feasibility of this step as mechanical vibrations under solution were already to cause significant nanowire movement. Spinning resists for the lift-off processes were therefore unlikely to work. Different approaches such as the pre-deposition of the clamping layer still creates problems with sub-micron alignment and precise etching requirements. Focused Ion Beam (FIB) deposition may be the favored technique since it can specifically deposit small amounts of gold to clamp down a nanowire. Nanowire assembly can survive the vacuum environments necessary for FIB and is a completely dry process compared to the numerous wet-processing steps by other methods. However, water adsorption from the assembly process may interfere with the deposition. Additionally, the process is expensive and particularly time-consuming with the clamping of several nanowires individually. Still, the tradeoffs favor FIB as compared to the other methods.

The growth of nanowires must also be improved in order to reduce its sensitivity to gas flow rate and pressure. A slight decrease in Ar/O_2 pressure can cause the oxygen content of the nanowire to drop significantly. A vacuum pump is one possible method to control the pressure inside the tube furnace. Separate Ar and O_2 sources can also be used to give a higher degree control over the oxygen content of the nanowire.

References

[1] O. Owen, V. Trapp, C. Skutches, M. Mozzoli, R. Hoeldtke, G. Boden, and G. Reichard Jr., "Acetone metabolism during diabetic ketoacidosis," Diabetes, Vol. 31, No. 3 (1982) pp. 242-248

[2] A. Wanekaya, W. Chen, N. Myung, and A. Mulchandani, "Nanowire-Based Electrochemical Biosensors," Electroanal., Vol. 18, No. 6 (2006) pp. 533-550

[3] M. Tanase, D. Silevitch, A. Hultgren, L. Bauer, P. Searson, G. Meyer, and D. Reich, "Magnetic trapping and self-assembly of multicomponent nanowires," J. Appl. Phys., Vol. 91, No. 10 (2002) pp. 8549-8551

[4] A. Salem, J. Chao, K. Leong, and P. Searson, "Receptor-Mediated Self-Assembly of Multi-Component Magnetic Nanowires," Adv. Mater., Vol. 16, No. 3 (2004) pp. 268-271

[5] M. Tanase, L. Bauer, A. Hultgren, D. Silevitch, L. Sun, D. Reich, P. Searson, and G. Meyer, "Magnetic Alignment of Fluorescent Nanowires," Nano Lett., Vol. 1, No. 3 (2001) pp. 155-158

[6] H. Pohl, "Dielectrophoresis: The behavior of neutral matter in nonuniform electric fields," Cambridge University Press, (1978)

[7] G. Eranna, B. Joshi, D. Runthala, and R. Gupta, "Oxide Materials for Development of Integrated Gas Sensors – A Comprehensive Review," Crit. Rev. Solid State, Vol. 29, No. 3-4 (2004) pp. 111-188

[8] J. Wu, H. Shih, W. Wu, Y. Tseng, and I. Chen, "Thermal evaporation growth and the luminescence property of TiO_2 nanowires," J. Crys. Growth, Vol. 281, No. 2-4 (2005) pp. 384-390 .

[9] J. Wu, W. Wu, and H. Shih, "Characterization of Single-Crystalline TiO_2 Nanowires Grown by Thermal Evaporation," J. Electrochem. Soc., Vol. 152, No. 8 (2005) pp. G613-G616

[10] J. Wu, H. Shih, and W. Wu, "Electron field emission from single crystalline TiO_2 nanowires prepared by thermal evaporation," Chem. Phys. Lett., Vol. 413, No. 4-6 (2005) pp. 490-494

[11] J. Wu, H. Shih, and W. Wu, "Formation and photoluminescence of single-crystalline rutile TiO_2 nanowires synthesized by thermal evaporation," Nanotechnology, Vol. 17, No. 1 (2006) pp. 105-109

[12] J. Lee, K. Park, T. Kim, H. Choi, and Y. Sung, "Controlled growth of high-quality TiO_2 nanowires on sapphire and silica," Nanotechnology, Vol. 17, No. 17 (2006) pp. 4317-4321

[13] A. Dupuis, L. Jodin, and E. Rouvière, "Catalytic growth of TiO_2 nanowires from a TiN thin film," Appl. Surf. Sci., Vol. 253, No. 3 (2006) pp. 1227-1235

[14] Y. Hu, O. Tan, W. Cao, and W. Zhu, "Fabrication and Characterization of Nano-sized $SrTiO_3$-Based Oxygen Sensor for Near Room-Temperature Operation," IEEE Sensors J., Vol. 5, No. 5 (2005) pp. 825- 832

[15] C. Xu, J. Tamaki, N. Miura, and N. Yamazoe, "Grain size effects on gas sensitivity of porous SnO_2-based elements," Sens. Actuat. B-Chem, Vol. 3, No. 2 (1991) pp. 147-155

[16] S. Morrison, "Semiconductor Gas Sensors," Sens. Actuat., Vol. 2 (1982) pp. 111-188

[17] J. Suehle, R. Cavicchi, M. Gaitan, and S. Semancik, "Tin oxide gas sensor fabricated using CMOS micro-hotplates and in-situ processing," IEEE Electr. Device L., Vol. 14, No. 3 (1993) pp. 118-120

[18] B. Panchapakesan, D. Devoe, M. Widmaier, R. Cavicchi, and S. Semancik, "Nanoparticle engineering and control of tin oxide microstructures for chemical microsensor applications," Nanotechnology, Vol. 12, No. 3 (2001) pp. 336-346

[19] B. Panchapakesan, R. Cavicchi, S. Semancik, and D. Devoe "Sensitivity, selectivity, and stability of tin oxide nanostructures on large area arrays of microhotplates," Nanotechnology, Vol. 17, No.. 2 (2006) pp. 415-425

[20] K.D. Benkstein and S. Semancik, "Mesoporous nanoparticle TiO_2 thin films for conductometric gas sensing on microhotplate platforms," Sens. Actuat. B-Chem., Vol. 113, No. 1 (2006) pp. 445-453

[21] S. Semancik, R. Cavicchi, M. Wheeler, J. Tiffany, G. Poirier, R. Walton, J. Suehle, B. Panchapakesan, and D. DeVoe, "Microhotplate platforms for chemical sensor research," Sensor Actuat. B-Chem, Vol. 77, No. 1-2 (2001) pp. 579-591

[22] A. Kolmakov, Y. Zhang, G. Cheng, and M. Moskovits, "Detection of CO and O2 Using Tin Oxide Nanowire Sensors," Adv. Mater., Vol. 15, No. 12 (2003) pp. 997-1000

[23] D.Barrettino, M. Graf, S. Taschini, S. Hafizovic, C. Hagleitner, and A. Hierlemann, "CMOS Monolithic Metal–Oxide Gas Sensor Microsystems," IEEE Sensors J.," Vol. 6, No. 2 (2006) pp. 276- 286

[24] J. Laconte, C. Dupont, A. Akheyar, J. Raskin, and D. Flandre, "Fully CMOS Compatible Low-Power Microheater," Proc. SPIE, Vol. 4755 (2002) pp. 634-644

[25] A. Kolmakov, D. Klenov, Y. Lilach, S. Stemmer, and M. Moskovits, "Enhanced Gas Sensing by Individual SnO_2 Nanowires and Nanobelts Functionalized with Pd Catalyst Particles," Nano Lett., Vol. 5, No. 4 (2005) pp. 667-673

[26] H. Wang, B. Kang, F. Ren, L. Tien, P. Sadik, D. Norton, S. Pearton, and J. Lin, "Hydrogen-selective sensing at room temperature with ZnO nanorods," Appl. Phys. Lett., Vol. 86, No. 24 (2005) pp. 243503-1 – 243503-3

[27] Q. Wan, Q. Li, Y, Chen, T. Wang, X. He, J. Li, and C. Lin, "Fabrication and ethanol sensing characteristics of ZnO nanowire gas sensors," Appl. Phys. Lett., Vol. 84, No. 18 (2004) pp. 3654-3656

[28] A. Narayanan, Y. Dan, V. Deshpande, N. Di Lello, S. Evoy, and S. Raman, "Dielectrophoretic Integration of Nanodevices With CMOS VLSI Circuitry," IEEE T. Nanotechnol., Vol. 5, No. 2 (2006) pp. 101-109

[29] Q. Li, Y. Liang, Q. Wan, and T. Wang, "Oxygen sensing characteristics of individual ZnO nanowire transistors," Appl. Phys. Lett., Vol. 85, No. 26 (2004) pp. 6389-6391

[30] M. Law, J. Goldberger, and P. Yang, "Semiconductor Nanowires and Nanotubes," Annu. Rev. Mater. Res., Vol. 34 (2004) pp. 83-122

[31] Z. Wang, "Novel Nanostructures and Nanodevices of ZnO," in Zinc Oxide Bulk, Thin Films and Nanostructures: Processing, Properties and Applications, ed. C. Jagadish and S. Pearton (Elsevier: London), 2006 pp. 339-70

[32] Y. Dan, Y. Cao, T. Mallouk, A. Johnson, S. Evoy, "Dielectrophoretically assembled polymer nanowires for gas sensing," Sens. Actuat. B-Chem, Vol. 125, No. 1 (2007) pp. 55-59

[33] R. Wagner and C. Ellis, "Vapor-Liquid-Solid Mechanism of Single Crystal Growth," Appl. Phys. Lett., Vol. 4, No. 89 (1964) pp. 89-90

[34] S. Park, S. Seo, S. Kim, and S. Han, "Surface roughness and strain effects on ZnO nanorod growth," Appl. Phys. Lett., Vol. 88. No. 251903 (2006) pp. 251903-1 – 251903-3

[35] C. Chang and C. Chang, "Growth of ZnO nanowires without Catalyst on Porous Silicon," Jpn. J. Appl. Phys., Vol. 43, No. 12 (2004) pp. 8360-8364

[36] P. Buffat and J. Borel, "Size effect on the melting temperature of gold particles," Phys. Rev. A, Vol. 13, No. 6 (1976) pp. 2287-2298

[37] M. Paulose, O. Varghese, C. Grimes, "Synthesis of Gold-Silica Composite Nanowires through Solid-Liquid-Solid Phase Growth," J. Nanosci. Nanotechno., Vol. 3, No. 4 (2003) pp. 341-346

[38] D. Bahloul-Hourlier and P. Perrot, "Thermodynamics of the Au-Si-O System: Application to the Synthesis and Growth of Silicon-Silicon dioxide Nanowires," J. Phase Equil. Diff., Vol. 28, No. 2 (2007) 150-157

[39] K. Hashimoto, H. Irie, and A. Fujishima, "TiO_2 Photocatalysis: A Historical Overview and Future Prospects," Jpn. J. Appl. Phys., Vol. 44, No. 12 (2005) pp. 8269-8285

[40] M. Nazeeruddin, A. Kay; I. Rodicio, R. Humphry-Baker, E. Mueller, P. Liska, N. Vlachopoulos, and M. Graetzel, "Conversion of light to electricity by cis-X2bis(2,2'-bipyridyl-4,4'-dicarboxylate)ruthenium(II) charge-transfer sensitizers (X = Cl-, Br-, I-, CN-, and SCN-) on nanocrystalline titanium dioxide electrodes," J. Am. Chem. Soc., Vol. 115 (1993) pp. 6382-6390

[41] C. Leung, M. Weinert, P. Allen, and R. Wentzcovitch, "First-principles study of titanium oxides," Phys. Rev. B, Vol. 54, No. 11 (1996) pp. 7857-7864

[42] S. Denker, "Electronic Properties of Titanium Monoxide," J. Appl. Physics, Vol. 37, No. 1 (1965) pp. p.142-149

[43] M. Hiratani, M. Kadoshima, T. Hirano, Y. Shimamoto, Y. Matsui, T. Nabatame, K. Torii, and S. Kimura, "Ultra-thin titanium oxide film with a rutile-type structure," Appl. Surf. Sci., Vol. 207, No. 1-4 (2003) pp. 13-19

[44] B. Predel, "Au-Ti (Gold-Titanium)," Landolt-Bornstein, Group IV Physical Chemistry - Phase Equilibria, Crystallographic and Thermodynamic Data of Binary Alloys, Volume 5 - Electronic Materials and Semiconductors, ed. O. Madelung, Springer (1991-1998)

[45] B. Xiang, Y. Zhang, Z. Wang, X. Luo, Y. Zhu, H. Zhang, and D. Yu, "Field-emission properties of TiO2 nanowire arrays," J. Phys. D. Appl. Phys., Vol. 38, No. 8 (2005) pp. 1152-1155

[46] H. Zhang, X. Luo, J. Xu, B. Xiang, and D. Yu "Synthesis of TiO2/SiO2 Core/Shell Nanocable Arrays," J. Phys. Chem. B, Vol. 108, No. 39 (2004) pp. 14866-14869

[47] J. Wu and C. Yu, "Aligned TiO2 Nanorods and Nanowalls," J. Phys. Chem. B., Vol. 108, No. 11 (2004) pp. 3377-3379

[48] S. Pradhan, P. Reucroft, F. Yang, and A. Dozier, "Growth of TiO2 nanorods by metalorganic chemical vapor deposition," J. Crys. Growth., Vol. 256, No. 1-2, 2003 pp. 83-88

[49] R. Plugaru, A. Cremades, and J. Piqueras, "Growth of titanium oxide nanorods," Semiconductor Conference, 2005. CAS 2005 Proceedings. 2005 International (2005) pp. 51-54

[50] T. Jones, "Electromechanics of particles," Cambridge University Press, (1995)

[51] J. Boote and S. Evans, "Dielectrophoretic manipulation and electrical characterization of gold nanowires," Nanotechnology, Vol. 16, No. 9 (2005) pp. 1500-1505

[52] A. Ramos, H. Morgan, N. Green, and A. Castellanos, "Ac electrokinetics: a review of forces in microelectrode structures" J. Phys. D. Appl. Phys., Vol. 31, No. 18 (1998) pp. 2338-2353

[53] Y. Liu, J. Chung, W. Liu, and R. Ruoff, "Dielectrophoretic Assembly of Nanowires," J. Phys. Chem. B., Vol. 110, No. 29 (2006) pp. 14098 -14106

[54] B. Lapizco-Encinas, B. Simmons, E. Cummings, and Y. Fintschenko, "Insulator-based dielectrophoresis for the selective concentration and separation of live bacteria in water," Electrophoresis, Vol. 25, No. 10-11 (2004) pp. 1695–1704

[55] B. Ozturk, C. Blackledge, B. Flanders, and D. Grischkowsky, "Reproducible interconnects assembled from gold nanorods," Appl. Phys. Lett., Vol. 88, No. 7 (2006) pp. 073108-1 – 073108-3

[56] R. Kretschmer and W. Fritzsche, "Pearl Chain Formation of Nanoparticles in Microelectrode Gaps by Dielectrophoresis," Langmuir, Vol. 20, No. 26 (2004) pp. 11797-11801

[57] D. Fan, F. Zhu, R. Cammarata, and C. Chien, "Efficiency of assembling of nanowires in suspension by ac electric fields," Appl. Phys. Lett., Vol. 89, No. 22 (2006) pp. 223115-1 – 223115-3

[58] R. Hamers, J. Beck, M. Erikkson, B. Li, M. Marcus, L. Shang, J. Simmons, and J. Streifer, "Electrically directed assembly and detection of nanowire bridges in aqueous media," Nanotechnology, Vol. 17, No. 11 (2006) pp. S280-S286

[59] R. Zhou, P. Wang, and H. Chang, "Bacteria capture, concentration and detection by alternating current dielectrophoresis and self-assembly of dispersed single-wall carbon nanotubes," Electrophoresis, Vol. 27, No. 7 (2006) pp. 1376-85

[60] S. Banerjee, B. White, L. Huang, B. Rego, S. O'Brien, and I. Herman, "Precise positioning of single-walled carbon nanotubes by ac dielectrophoresis," J. Vac. Sci. Technol. B, Vol. 24, No. 6 (2006) pp. 415-419

[61] P. Smith, C. Nordquist, T. Jackson, T. Mayer, B. Martin, J. Mbindyo, T. Mallouk, "Electric-field assisted assembly and alignment of metallic nanowires," Appl. Phys. Lett., Vol. 77, No. 9 (2000) pp. 1399-1401

[62] C. Lao, J. Liu, P. Gao, L. Zhang, D. Davidovic, R. Tummala, and Z. Wang, "ZnO Nanobelt/Nanowire Schottky Diodes Formed by Dielectrophoresis Alignment across Au Electrodes," Nano Lett., Vol. 6, No. 2 (2006) pp. 263-266

[63] S. Lee and R. Bashir, "Dielectrophoresis and Chemically Mediated Directed Self-Assembly of Micrometer-Scale Three-Terminal Metal Oxide Semiconductor Field-Effect Transistors," Adv. Mater., Vol. 17, No. 22 (2005) pp. 2671-2677

[64] A. Wissner-Gross, "Dielectrophoretic reconfiguration of nanowire interconnects," Nanotechnology, Vol. 17, No. 19 (2006) pp. 4986-4990

[65] T. Kim, S. Lee, N. Cho, H. Seong, H. Choi, S. Jung, and S. Lee, "Dielectrophoretic alignment of gallium nitride nanowires (GaN NWs) for use in device applications," Nanotechnology, Vol. 17. No. 14 (2006) pp. 3394-3399

[66] A. Motayed, M. He, and A. Davydov, "Realization of reliable GaN nanowire transistors utilizing dielectrophoretic alignment technique," J. Appl. Phys., Vol. 100, No. 11 (2006) pp. 114310-1 – 114310-9

[67] D. Clauge and E. Wheeler, "Dielectrophoretic manipulation of macromolecules: The electric field," Phys. Rev. E, Vol. 64, No. 2 (2001) pp. 026605-1 – 026605-8

[68] M. Dimaki and P. Bøggild, "Dielectrophoresis of carbon nanotubes using microelectrodes: a numerical study," Nanotechnology, Vol. 15, No. 8 (2004) pp. 1095-1102

[69] D. Chen, H. Du, W. Li, and C. Shu, "Numerical modeling of dielectrophoresis using a meshless approach," J. Micromech. Microeng., Vol. 15, No. 5 (2005) pp. 1040-1048

[70] H. Zhou, R. Tilton, and L. White, "The role of electrode impedance and electrode geometry in the design of microelectrode systems," J. Colloid Interf. Sci., Vol. 297, No. 2 (2006) pp. 819-831

[71] "Vapor Pressure of the Elements – Data," in *CRC Handbook of Chemistry and Physics, 88th Edition (Internet Version 2008),* David R. Lide, ed., CRC Press/Taylor and Francis, Boca Raton, FL.

[72] "Vapor Pressure of the Elements – Equations," in *CRC Handbook of Chemistry and Physics, 88th Edition (Internet Version 2008),* David R. Lide, ed., CRC Press/Taylor and Francis, Boca Raton, FL.

[73] "Thermal and Physical Properties of Pure Metals," in *CRC Handbook of Chemistry and Physics, 88th Edition (Internet Version 2008)*, David R. Lide, ed., CRC Press/Taylor and Francis, Boca Raton, FL.

[74] S. Shankar, A. Rai, B. Ankamwar, A. Singh, A. Ahmad, and M. Sastry, "Biological synthesis of triangular gold nanoprisms," Nat. Mater., Vol. 3, No. 7 (2004) pp. 482-488

[75] A. Courty, A. Henry, N. Goubet, and M. Pileni, "Large triangular single crystals formed by mild annealing of self-organized silver nanocrystals," Nat. Mater., Vol. 6, No. 11 (2007) pp. 900-907

[76] W. Jun, C. Mitchell, R. Egdell, and J. Foord, "Real time STM observation of Au-assisted decomposition of SiO_2 films on Si(111) at elevated temperatures," Surf. Sci., Vol. 506, No. 1-2 (2002) pp. 66-79

[77] M. Liehr, J. Lewis, and G. Rubloff, "Kinetics of high-temperature thermal decomposition of SiO_2 on Si(100)," J. Vac. Sci. Technol. A, Vol. 5, No. 4 (1987) pp.1559-1562

[78] H. Dallaporta, M. Liehr, and J. Lewis, "Silicon dioxide defects induced by metal impurities," Phys. Rev. B, Vol. 41, No. 8 (1990) pp.5075-5083

[79] D. Al-Mawlawi, C. Liu, and M. Moskovits, "Nanowires formed in anodic oxide nanotemplates," J. Mater. Res., Vol. 9, No. 4 (1994) pp. 1014-1018

[80] C. Martin, "Membrane-Based Synthesis of Nanomaterials," Chem. Mater., Vol. 8, No. 8 (1996) pp. 1739-1746

[81] B. Martin, D. Dermondy, B. Reiss, M. Fang, L. Lyon, M. Natan, and T. Mallouk, "Orthogonal Self-Assembly on Colloidal Gold-Platinum Nanorods," Adv. Mater, Vol. 11. No. 12 (1999) pp. 1021-1025

[82] M.T. Chen, and J. Ting, "Sputter deposition of ZnO nanorods/thin-film structures on Si," Thin Solid Films, Vol. 494, No. 1-2 (2006) pp. 250-254

[83] "Electrical conductivity of water," in *CRC Handbook of Chemistry and Physics, 88th Edition (Internet Version 2008),* David R. Lide, ed., CRC Press/Taylor and Francis, Boca Raton, FL.

[84] "Permittivity (Dielectric Constant) of water at various frequencies," in *CRC Handbook of Chemistry and Physics, 88th Edition (Internet Version 2008),* David R. Lide, ed., CRC Press/Taylor and Francis, Boca Raton, FL.

[85] "Electrical resistivity of pure metals," in *CRC Handbook of Chemistry and Physics, 88th Edition (Internet Version 2008),* David R. Lide, ed., CRC Press/Taylor and Francis, Boca Raton, FL.

[86] K. Ellmer, "Resistivity of polycrystalline zinc oxide films: current status and physical limit," J. Phys. D. Appl. Phys., Vol. 34, No. 21 (2001) pp. 3097-3108